PHOTONICS Research

Performance improvement approaches for optical fiber SPR sensors and their sensing applications

Jianying Jing,[1,2,3] Kun Liu,[1,2,3,*] Junfeng Jiang,[1,2,3] Tianhua Xu,[1,2,3] Shuang Wang,[1,2,3] Jinying Ma,[1,2,3] Zhao Zhang,[1,2,3] Wenlin Zhang,[1,2,3] and Tiegen Liu[1,2,3]

[1]School of Precision Instruments and Opto-Electronics Engineering, Tianjin University, Tianjin 300072, China
[2]Key Laboratory of Opto-Electronics Information Technology, Ministry of Education, Tianjin University, Tianjin 300072, China
[3]Tianjin Optical Fiber Sensing Engineering Center, Institute of Optical Fiber Sensing, Tianjin University, Tianjin 300072, China
*Corresponding author: beiyangkl@tju.edu.cn

Received 22 September 2021; revised 1 November 2021; accepted 1 November 2021; posted 2 November 2021 (Doc. ID 439861); published 16 December 2021

Optical fiber surface plasmon resonance (SPR) sensors point toward promising application potential in the fields of biomarker detection, food allergen screening, and environmental monitoring due to their unique advantages. This review outlines approaches in improving the fiber SPR sensing performance, e.g., sensitivity, detection accuracy, reliability, cross-sensitivity, selectivity, convenience and efficiency, and corresponding sensing applications. The sensing principles of SPR sensors, especially the performance indicators and their influencing factors, have been introduced. Current technologies for improving the fiber SPR performance and their application scenarios are then reviewed from the aspects of fiber substrate, intrinsic layer (metal layer), and surface nanomaterial modification. Reasonable design of the substrate can strengthen the evanescent electromagnetic field and realize the multi-parameter sensing, and can introduce the *in situ* sensing self-compensation, which allows corrections for errors induced by temperature fluctuation, non-specific binding, and external disturbances. The change of the intrinsic layer can adjust the column number, the penetration depth, and the propagation distance of surface plasmon polaritons. This can thereby promote the capability of sensors to detect the large-size analytes and can reduce the full width at half-maximum of SPR curves. The modification of various-dimensionality nanomaterials on the sensor surfaces can heighten the overlap integral of the electromagnetic field intensity in the analyte region and can strengthen interactions between plasmons and excitons as well as interactions between analyte molecules and metal surfaces. Moreover, future directions of fiber SPR sensors are prospected based on the important and challenging problems in the development of fiber SPR sensors.

https://doi.org/10.1364/PRJ.439861

1. INTRODUCTION

Nomenclature

Abbreviation	Full name
2-D	Two-dimensional
3-D	Three-dimensional
AET	2-aminoethanethiol
AgNW-OF	Ag nanowires and tapered optical fiber
ATR	Attenuated total reflection
AuNPs	Au nanoparticles
BP	Black phosphorus
BSA	Bovine serum albumin
CNTs	Carbon nanotubes
CPWR	Coupled plasmon waveguide resonance
Cs/PSS	Chitosan/polysodium styrene sulfonate
CuNPs	Cuprum nanoparticles
DA	Detection accuracy
DE	Distal ends
DML	Dielectric matching layer
ELP	Electroless plating
ERY	Erythromycin
EW	Evanescent wave
FOM	Figure of merit
FWHM	Full width at half-maximum
GNP	Graphene nanoplatelet
GO	Graphene oxide
HCF	Hollow-core fiber
HGNPs	Hollow gold nanoparticles
IgG	Immunoglobulin G
ITO	Indium tin oxide
LOD	Limit of detection
LOQ	Limit of quantification
LPFG	Long period fiber grating
LRSPPs	Long range surface plasmon polaritons
LRSPR	Long range surface plasmon resonance

(Table continued)

(Table continued)

Abbreviation	Full name
LS	Lateral surface
LSPR	Localized surface plasmon resonance
MMF	Multi-mode fiber
MWCNTs	Multi-walled carbon nanotubes
NGWSPR	Nearly guided wave surface plasmon resonance
PBA	Pyrene-1-boronic acid
PCF	Photonic crystal fiber
PDA	Polydopamine
PDMS	Polydimethylsiloxane
PdNPs	Palladium nanoparticles
PMBA	P-mercaptophenylboronic acid
PtNPs	Platinum nanoparticles
PTOF	Polymer-tipped optical fiber
QF	Quality factor
rGO	Reduced graphene oxide
RI	Refractive index
SEM	Scanning electron microscopy
SERS	Surface enhanced Raman scattering
SLR	Surface lattice resonance
SMF	Single-mode fiber
SNR	Signal to noise ratio
SPF	Side-polished fiber
SPPs	Surface plasmon polaritons
SPR	Surface plasmon resonance
SWCNTs	Single-walled carbon nanotubes
TE	Transverse electric
TFBG	Tilted fiber Bragg grating
TM	Transverse magnetic
TMDCs	Transition metal dichalcogenides
WCSPR	Waveguide coupled surface plasmon resonance
XO	Xanthine oxidase

Surface plasmon resonance (SPR) sensing methods can realize analyses of biomolecular interactions with high sensitivity, rapid response, and no labeling [1–3]. Optical fiber-based SPR effect can be regarded as the nonlinear multiple integral of the prism-based SPR effect at the incident angle and the incident plane. Optical fiber SPR sensors possess the advantages of anti-electromagnetic interference, corrosion resistance, small volume, and great flexibility, and they can easily form a sensor network through cascading or other manners. This allow us to achieve the real-time, online, remote, and multi-parameter detection of target analytes [4,5]. Therefore, the research on fiber SPR sensors has made significant progress in the field of biochemical sensing. However, on the one hand, the size of viruses, cells, proteins, nucleic acids, and some other biological macromolecules is in the order of micrometers or even millimeters and is much larger than the penetration depth of surface plasmon polaritons (SPPs), which is on a scale of hundreds of nanometers [6,7]. This indicates that the above substances cannot be detected sensitively via conventional SPR sensors. On the other hand, the full width at half-maximum (FWHM) of conventional SPR sensors is relatively large, which exceeds 100 nm, and will result in a low detection accuracy (DA). Furthermore, the detection repeatability and the anti-interference capability of conventional SPR sensors need to be improved. Therefore, performance improvement approaches for fiber SPR sensors have been widely studied and are mainly categorized into the following three branches.

Reasonable and flexible design of fiber substrates by means of cascading, polishing, and other methods can increase the evanescent field leakage and can introduce the *in situ* interference self-compensation function. This will promote the capability of sensors in detecting the variety and the intensity of external factors.

Adjusting intrinsic layers (metal layers) of fiber SPR sensors can modulate the original light field, which makes sensors suitable for different application scenarios. Attenuated total reflection (ATR)-based long range SPR (LRSPR) [8,9], coupled plasmon waveguide resonance (CPWR) [10,11], nearly guided wave SPR (NGWSPR) [11], and waveguide coupled SPR (WCSPR) [12] can be considered as optimization parameters to improve the performance of conventional SPR sensors from different aspects.

The modification of various-dimensionality nanomaterials with high refractive index (RI) on the sensor surfaces by physical sputtering or chemical bond coupling can cause large disturbance of the evanescent field [9,13], can strengthen the confined electric field intensity [11], and can promote the capability of sensors for detecting small changes in the ambient environment.

According to above discussions, an overview of performance improvement approaches for fiber SPR sensors and their sensing applications is presented. There have been some reviews on SPR, but they are different from our report in terms of research scope and focus. In 2011, Shalabney *et al.* [11] classified sensitivity-enhancement techniques focused on the prism coupling-type SPR sensors. Fiber SPR sensors can be regarded as one more dimension than prism-based SPR sensors due to the multiple incident angles of light and the curved incident surface. Therefore, the fiber SPR effect focused in our paper is obviously different from the reported prism SPR effect in Ref. [11], and more performance indicators are involved in our review paper.

Optical fiber SPR sensors based on commercial fibers, customized fiber structures, and metastructure platform have been outlined in Refs. [14–19], but they are more focused on the classification of fiber SPR sensors. Meanwhile, applications of fiber SPR sensors in various scenarios (e.g., environmental monitoring, food safety detection, and biological immunoassay) have also been involved in Refs. [15,16,20–23]. Both classification and application scenarios are obviously different from the performance improvement approaches discussed in our paper. In addition, the sensing mechanism and applications of specific types of fiber SPR sensors (e.g., D-type fiber SPR sensors, hybrid plasmonic fiber sensors, molecular imprinting improved fiber SPR sensors, and surface plasmon cavities) have been systematically reviewed in Refs. [24–30]. The focuses of these reviews are particular, which are different from the broader focuses of our paper. We hope that this review can provide an insightful overview of fiber SPR sensors and inspirations for the development of SPR sensors.

2. THEORETICAL FOUNDATION OF FIBER SPR SENSORS

A. Sensing Mechanism of Fiber-Based SPR

The disassembly of cylindrical surfaces in the optical fiber allows the SPR phenomenon at each point to be explained

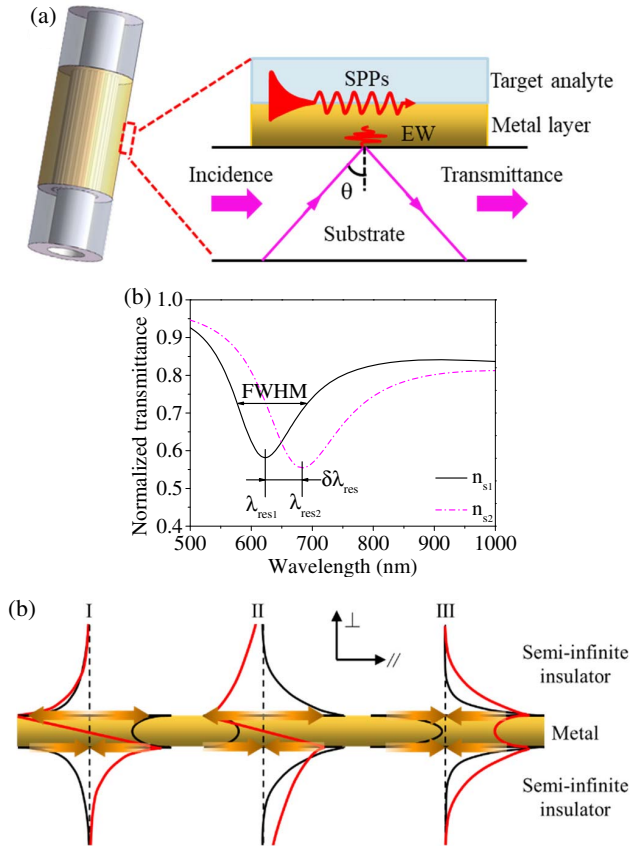

Fig. 1. (a) The layer configuration and (b) resonance spectrum of SPR sensor. (c) Field/current distributions of the insulator-metal-insulator model corresponding to SPR sensing structure [31]. Note: I, II, and III are three modes with the lowest loss; red line, black line, and orange arrow represent electric field distribution, magnetic field distribution, and current conduction, respectively.

by a three-layer structure. As shown in Fig. 1(a), the layer configuration of a traditional SPR sensor consists of a substrate layer, an intrinsic layer, and a dielectric layer. The substrate can employ commercial fibers (e.g., multi-mode fiber (MMF) [32], photonic crystal fiber (PCF) [33], hollow-core fiber (HCF) [34]), customized fiber such as suspended-core fiber [35], and the fiber grating (e.g., tilted fiber Bragg grating (TFBG) [5], long period fiber grating (LPFG) [36]). The intrinsic layer utilizes materials, with negative real-part and positive imaginary-part in dielectric constants, such as mono/bimetallic film with high reflectivities and low absorption rates (e.g., Au [37], Ag [38], Cu [39], Al [40]). The dielectric layer refers to the analyte layer.

The total reflection will occur when the transverse magnetic (TM) polarized light is projected on the substrate-metal layer interface at an angle larger than the critical value. The resulted evanescent wave (EW) enters the metal layer, and its energy decreases exponentially. This excites SPPs to propagate along the upper surface of the metal layer [7,11]. When wave vector components of the EW and SPPs on the interface are equal, SPPs will be strongly coupled with the EW. At this point, most of the energy of the incident light is coupled into SPPs [14] while a resonance dip appears in the transmission spectrum, as shown in Fig. 1(b). This phenomenon is called SPR. The SPP mode, which is strongly coupled to the EW, is called the resonance SPP mode, i.e., SPR mode. The SPP mode that is weakly coupled to the evanescent wave is called the non-resonance SPP mode. The wavelength of the incident light, which corresponds to the occurrence of the strong coupling, is defined as the resonance wavelength (λ_{res}). When the RI of the dielectric on the metal layer surface changes, a new resonance will occur for the incident light at another angular frequency. This can be macroscopically manifested in the change of the resonance wavelength. According to the change of the resonance wavelength, we can measure the change in the average RI of the dielectric on the metal layer surface, which is caused by the change of a merging of parameters belonging to bulk/volume sensing and others belonging to surface sensing, to realize the detection of the analyte.

B. Performance Indicators of Fiber SPR Sensors and Their Influencing Factors

The performance improvement of fiber SPR sensors mainly is targeted at some indicators, and this section introduces the typical performance indicators of the sensor and their influencing factors. Since it is not convenient to adjust the incident angle at the fiber core-cladding interface, most fiber SPR sensors are designed based on the wavelength scanning. The depth of the resonance dip is determined by the energy coupling between the resonance SPP modes and the evanescent wave. The stronger the coupling is, the deeper the resonance dip will be. The FWHM of resonance dip is determined by the difference between the resonance SPP modes-evanescent wave coupling and the non-resonance SPP modes-evanescent wave coupling. The greater the difference is, the narrower the FWHM will be. Meanwhile, some researchers claim that the observed SPR curve band is the result of the convolution of the resonance dips excited by separate optical modes [41], and the Ohmic loss of metal and the radiative loss of SPPs on the parallel axis [in Fig. 1(c)] lead to the broadening of the resonance dip [11].

The sensitivity ($S_{\lambda n}$) of the sensor is defined as the resonance wavelength shift ($\partial\lambda_{res}$) caused by the unit average RI change (∂n_s) surrounding the sensing region, as expressed in Eq. (1) [42]. Its magnitude mainly depends on the overlap integral of the SPP electric field intensity on the vertical axis, as shown in Fig. 1(c), in the analyte region [11]. The DA is defined as the reciprocal of the FWHM value in the resonance dip, as expressed in Eq. (2) [42]. Some research works also employ the depth-width ratio in the SPR curve to describe the DA [43]. Both definitions have similar properties. The narrower the FWHM is, the easier it is to find the resonance wavelength and the higher the DA is. The signal to noise ratio (SNR) is inversely proportional to the FWHM, as expressed in Eq. (3) [44]. The figure of merit (FOM) and the quality factor (QF) are comprehensively quantitative indicators for characterizing the performance of the sensor, as expressed in Eqs. (4) and (5) [45], respectively.

The limit of detection (LOD) of the sensor represents the minimum concentration or the quantity of the target components that can be detected from the test sample within a given

Table 1. Parameter Indices to Evaluate the Performance of SPR Sensors

Index	Equation		Parametric Meaning	Ref.
$S_{\lambda n}$	$S_{\lambda n}=\frac{\partial\lambda_{\text{res}}}{\partial n_s}$	(1)	∂n_s and $\partial\lambda_{\text{res}}$ represent the change of external average RI and the resonance wavelength shift caused by ∂n_s, respectively.	[42]
DA	$\text{DA}=\frac{1}{\text{FWHM}}$	(2)	–	
SNR	$\text{SNR}=\frac{\delta\lambda_{\text{res}}}{\text{FWHM}}$	(3)	$\delta\lambda_{\text{res}}$ represents the resonance wavelength shift caused by the change of external average RI.	[44]
FOM	$\text{FOM}=\frac{S_{\lambda n}}{\text{FWHM}}$	(4)	–	[45]
QF	$\text{QF}=\frac{\delta\lambda_{\text{res}}}{\text{FWHM}}\times S_{\lambda n}$	(5)	–	
	$\text{LOD}=\frac{\Delta\lambda}{S_{\lambda n}}$	(6)	$\Delta\lambda$ represents the wavelength resolution of the spectrometer.	[46–48]
LOD	$y_{\text{LOD}}=\bar{y}_{\text{blank}}+t_{\alpha,k-1}\sigma_y$,	(7)	$\bar{y}_{\text{blank}}$ represents the average signal obtained by repeated measurements of the blank sample. $t_{\alpha,k-1}$ represents the α-quantile of Student's t-function with $k-1$ degrees of freedom. σ represents the standard deviation.	
	$x_{\text{LOD}}=f^{-1}(\bar{y}_{\text{blank}}+3\sigma_{\max})$	(8)		
LOQ	$\text{LOQ}=\frac{\delta\lambda}{S_{\lambda n}}$	(9)	$\delta\lambda=i\sigma$, i, and σ represent positive integer and the standard deviation in resonance wavelength near blank concentration, respectively.	[46]

degree of reliability. Equations (6)–(8) [46–48] display the different ways to evaluate LOD. Slightly different from LOD, the limit of quantification (LOQ) represents the lowest detectable analyte concentration near blank considering the standard deviation of calibration curve, as expressed in Eq. (9) [46]. In general, the kinetic adsorption curve, acquired from biomass detection by using the sensor, is obtained by fitting the Langmuir adsorption isotherm equation [49] or logistic regression equation [50]. The sensitivity ($S_{\lambda n}$) utilized to calculate the LOD and the LOQ can be obtained via the first-order derivative or the linear fitting of the low-concentration data (near zero) in the adsorption curve [46,47,51]. The aforementioned performance indicators of SPR sensors are listed in Table 1.

3. PERFORMANCE IMPROVEMENT APPROACHES FOR FIBER SPR SENSORS AND THEIR SENSING APPLICATIONS

A. Reasonable Design of Fiber Substrate to Improve Sensor Performance

1. Increasing the Evanescent Field Leakage to Amplify SPR Signal

The use of different commercial optical fibers as the substrate to construct SPR sensors will obtain different sensing characteristics. PCF-based SPR sensors possess high sensitivity due to the high confinement loss of SPPs excited by a Gaussian-like leaky mode of the PCF element [15]. HCF-based SPR sensors can realize all-fiber distributed sensing, since the entire inner wall of the fiber can be coated with chemicals to form the sensing area [34]. Fiber grating-based SPR sensors can obtain a smaller FWHM and a higher SNR [36].

SPR is the electromagnetic resonance stimulated by the evanescent field leakage when the total reflection occurs at the substrate interface. Therefore, research works are carried out to increase the evanescent field leakage for enhancing the sensitivity by customizing the fiber structure through micro/nano processing (e.g., fused tapering [52], side polishing [53], bending into U-shape [54]). In 2014, Cennamo *et al.* [55] fabricated a tapered plastic fiber SPR sensor, of which the specific sensing structure is shown in Fig. 2(a). When the light enters the tapered gradient region, it will be diffused into the cladding due to the reduction of the core diameter. At this point, fundamental modes in the core become high-order modes, and the light in the cladding is more likely to excite the evanescent wave on the metal layer [14]. The resonance spectra obtained in such a sensor to detect nicotine are shown in Figs. 2(b) and 2(c). The sensitivity and the LOD of the sensor achieved 1.3×10^4 nm/M and 1.86×10^{-4} M (1 M = 1 mol/L), respectively.

When the cladding and even the core of the fiber on one side are polished away, the evanescent field energy will leak from the polished area. This allows the side-polished fiber (SPF)-based SPR sensor to have a higher sensitivity [53]. In 2009, Tsai *et al.*

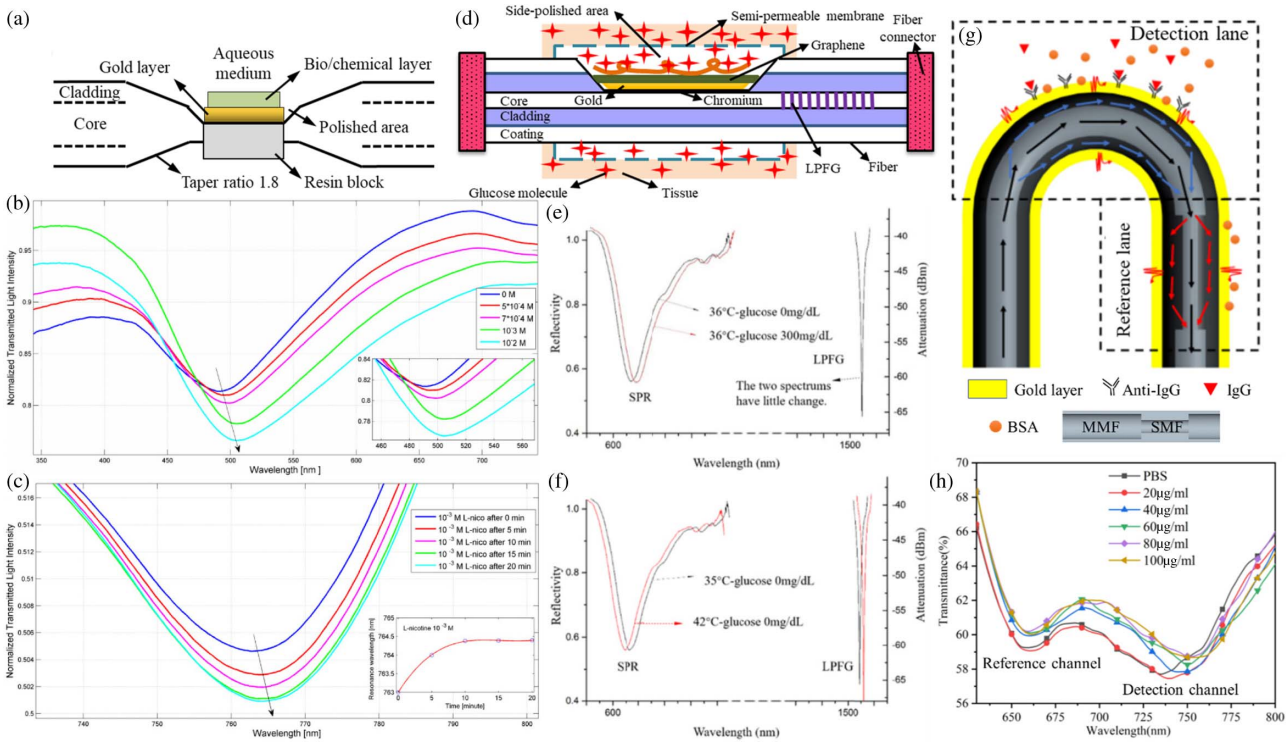

Fig. 2. (a) Schematic of the sensing structure and (b) concentration response as well as (c) time response spectra for the nicotine detection using the tapered plastic fiber SPR sensor [55]. (d) Schematic of the sensing structure and (e) glucose concentration response as well as (f) temperature response spectra of the SPF-SPR sensor [56]. (g) Schematic of the sensing structure and (h) human IgG concentration response spectra of the U-shaped fiber SPR sensor [57].

[58] proposed a TM mode field coupling-based multi-step SPF-SPR sensor. The polished area consisted of three Au layer coated areas, leading to a two fold sensitivity enhancement, compared to the sensor with a single Au layer coated area.

2. Multi-Parameter Sensing

The signal spectral response of the fiber SPR sensor has a wide wavelength range; and thus, multi-parameter sensing can be realized by capturing different central wavelengths in different bands [59,60]. The implementations are mainly categorized into the following three branches. First, multiple detection lanes are constructed based on different fiber substrates [61–65]. In 2021, Xiao *et al.* [61] developed a fiber SPR sensor with three detection lanes through coating Au-graphene composite layer on the surface of the side-polished PCF and filling two air holes with magnetic fluid and polydimethylsiloxane (PDMS), respectively, as shown in Fig. 3(a). Since the resonance conditions in the measurement of the three lanes were satisfied in different bands, the loss spectrum of the sensor contained three peaks, which were used for the measurement of magnetic field, RI, and temperature, respectively, as shown in Fig. 3(b). Multi-parameter detection can also be realized via constructing multiple detection lanes based on different mechanisms, e.g., localized SPR (LSPR) and interferometric sensing [68], as well as, birefringence phenomenon [69].

Second, double detection lanes are constructed in the same sensing area [66,70]. In 2019, Alonso-Murias *et al.* [66] achieved three-parameter measurement by coating PDMS onto part of the Au layer covered area in the SPR fiber tip sensor, as shown in Fig. 3(c). The segment coated with PDMS was used for the measurement of temperature, and the bare part was used for the measurement of RI and liquid level. The response signal in the liquid level measurement was reflected based on the intensity modulation, and the other two were expressed based on the wavelength modulation, as shown in Fig. 3(d).

Thirdly, multi-parameter measurement is carried out based on the sensitive characteristics of dielectric materials [67,71]. In 2020, Wang *et al.* [67] developed a fiber LRSPR sensor based on the dielectric buffer layer with temperature-sensitive photoabsorption characteristic, as shown in Fig. 3(e), where the dual-parameter measurement of RI and temperature was realized. The buffer layer had an absorption effect on light near 350 nm, and the absorption intensity decreased with the increase of the temperature. Therefore, the transmission spectrum of the sensor contained a characteristic absorption peak and a long-range resonance dip, as shown in Fig. 3(f).

The optical fiber sensors used for multi-parameter measurement can meet the needs of different complex scenarios, which is of great significance to application.

3. Self-Compensation for Temperature Fluctuation

Multi-parameter measurement is generally used to solve the cross-influence among parameters. In 2019, Zhang *et al.* [56] developed an SPF-SPR sensor, and the sensing structure is shown in Fig. 2(d). A segment of LPFG was embedded in the SPF to realize the self-compensation for temperature. The

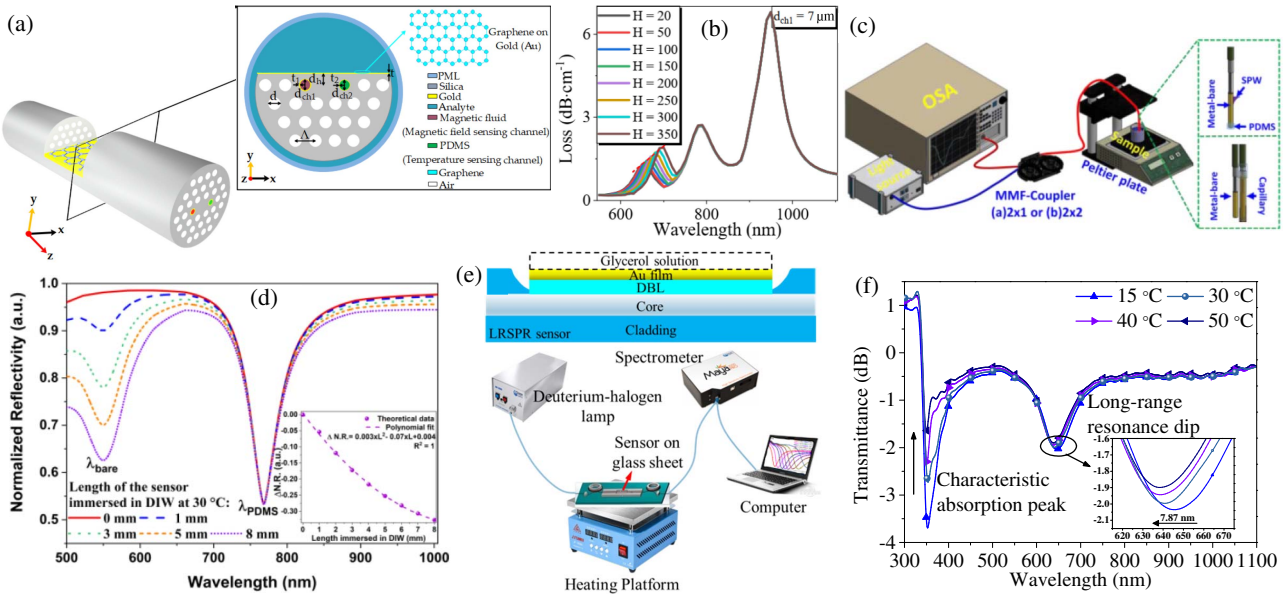

Fig. 3. (a) Schematic of the PCF-SPR sensor for the simultaneous measurement of magnetic field, RI, and temperature [61]. (b) Loss spectrum of the PCF-SPR sensor for the measurement of magnetic field [61]. (c) Schematic of the experimental setup for the characterization process of the SPR fiber tip sensor [66]. (d) Transmission spectrum of the SPR fiber tip sensor for the measurement of the liquid level [66]. (e) Schematic of the LRSPR sensor and experimental setup for the simultaneous measurement of RI and temperature [67]. (f) Transmission spectrum of the LRSPR sensor for the measurement of temperature [67].

produced sensor was applied to detect the concentration and the temperature of the glucose, and the obtained transmission spectra are shown in Figs. 2(e) and 2(f). The relationship between the wavelength shift ($\Delta\lambda_{res}$) in the SPR resonance dip and the change in the concentration (ΔC) and the temperature (ΔT) of the glucose is given as follows:

$$\Delta\lambda_{res} = K_{Ca} \cdot \Delta C + K_{Ta} \cdot \Delta T. \tag{10}$$

The relationship between the wavelength shift in the optical grating resonance peak ($\Delta\lambda_{LPFG}$) and the change in the concentration (ΔC) and the temperature (ΔT) of the glucose is given as follows:

$$\Delta\lambda_{LPFG} = K_{Cb} \cdot \Delta C + K_{Tb} \cdot \Delta T, \tag{11}$$

where K_{Ca} and K_{Ta} are the sensitivity coefficients of the resonance dip for detecting the concentration and the temperature of the glucose, respectively. $K_{Cb} = 0$ and K_{Tb} are the sensitivity coefficients of the resonance peak for detecting the concentration and the temperature of the glucose, respectively. Combining Eqs. (10) and (11), the following relation matrix can be obtained:

$$\begin{bmatrix} \Delta C \\ \Delta T \end{bmatrix} = \begin{bmatrix} K_{Ca} & K_{Ta} \\ 0 & K_{Tb} \end{bmatrix}^{-1} \begin{bmatrix} \Delta\lambda_{res} \\ \Delta\lambda_{LPFG} \end{bmatrix}. \tag{12}$$

According to Eq. (12), the resonance wavelength shift caused by the change in the concentration and the temperature of the glucose can be calculated separately. Meanwhile, the SPR sensing unit and the LPFG temperature compensation unit were set close to each other, and thus the sensor could realize the *in situ* temperature self-compensation in the detection of the glucose concentration.

Similarly, Weng *et al.* [72] implemented a double-SPF-SPR sensor, which contained two polished areas in 2016. The temperature and the RI sensitivities in the *X*-pol loss spectrum were 0.1371 nm/°C and 561.4286 nm/RIU, and the temperature and the RI sensitivities in the *Y*-pol loss spectrum were 0.04736 nm/°C and 457.1429 nm/RIU, respectively. The sensor theoretically eliminated the measurement errors caused by the fluctuation of the ambient temperature in the measurement of RI.

4. Self-Compensation for Non-Specific Binding

When the fiber SPR sensor is employed to detect the biomass based on the antigen-antibody specific binding, the resonance wavelength shift caused by the interaction between the antigen and the non-specific binding site on the sensor surface will affect the detection reliability. In 2021, Wang *et al.* [57] realized a U-shaped fiber SPR sensor, as shown in Fig. 2(g). When the light passed through the bending part, part of the light would no longer meet the condition of the total reflection and would leak into the cladding due to the bending of the fiber core. Meanwhile, the cladding was also bent. The light that met the total reflection condition in the cladding can stimulate the SPR, and the light that did not meet the condition would leak to the ambient environment and would strengthen the evanescent field [14]. The sensing region is divided into the antibody modified detection lane constructed by the MMF and the unmodified reference lane constructed by the SMF. The sensor was applied for the detection of RI and human immunoglobulin G (IgG) solution doped with bovine serum albumin (BSA). Two resonance dips appeared in the transmission spectrum, as shown in Fig. 2(h), corresponding to the two lanes. The influence of the non-specific adsorption of BSA on

the detection branch can be calculated according to the wavelength shift of the reference lane, as expressed in Eq. (13):

$$\Delta\lambda_d = \Delta\lambda_r \times S_d/S_r, \tag{13}$$

where $\Delta\lambda_d$ and $\Delta\lambda_r$ are wavelength shifts of the detection lane and the reference lane, respectively, and S_d and S_r are RI sensitivities of the detection lane and the reference lane, respectively. Therefore, the introduction of the reference lane can theoretically eliminate the measurement errors caused by the non-specific binding of BSA in the IgG detection in the detection lane. Furthermore, similar to the terminal reflective sensing structure [73,74], the U-shaped fiber SPR sensor allows an easy operation since it can be directly inserted into the analyte solution.

Similarly, Wang *et al.* [75] developed a cascaded dual-lane optical fiber SPR biosensor, consisting of an Au layer coated detection lane and an Ag layer coated reference lane, in 2020. The resonance dip positions corresponding to the two lanes were different, and the sensor can theoretically eliminate the measurement errors caused by the non-specific binding and the temperature cross-sensitivity. When the sensor, of which the transmission spectrum contains multiple resonance dips, is exposed to the external mechanical interference, the entire resonance spectrum will exhibit a shift, but the relative wavelength difference between the resonance dips remains unchanged. In this case, the sensor provides an *in situ* sensing self-reference function, and this leads to a higher detection reliability [13,76].

B. Attenuated Total Reflection-Based SPR Modes

1. Long Range SPR

LRSPR refers to an electromagnetic resonance mode stimulated by adding a lossless dielectric buffer layer (e.g., Cytop [9], Teflon [77], MgF_2 [78], nano-SiO_2 film [79]), with an RI similar to that of the intended buffer layer but lower than that of the substrate, between the substrate and the metal layer. The layer configuration is shown in Fig. 4(a). Compared with the traditional SPR sensor, in which there only exists a single row of SPPs, the SPPs in the LRSPR sensor exist on both sides of the metal layer. The constructive interference between the two rows

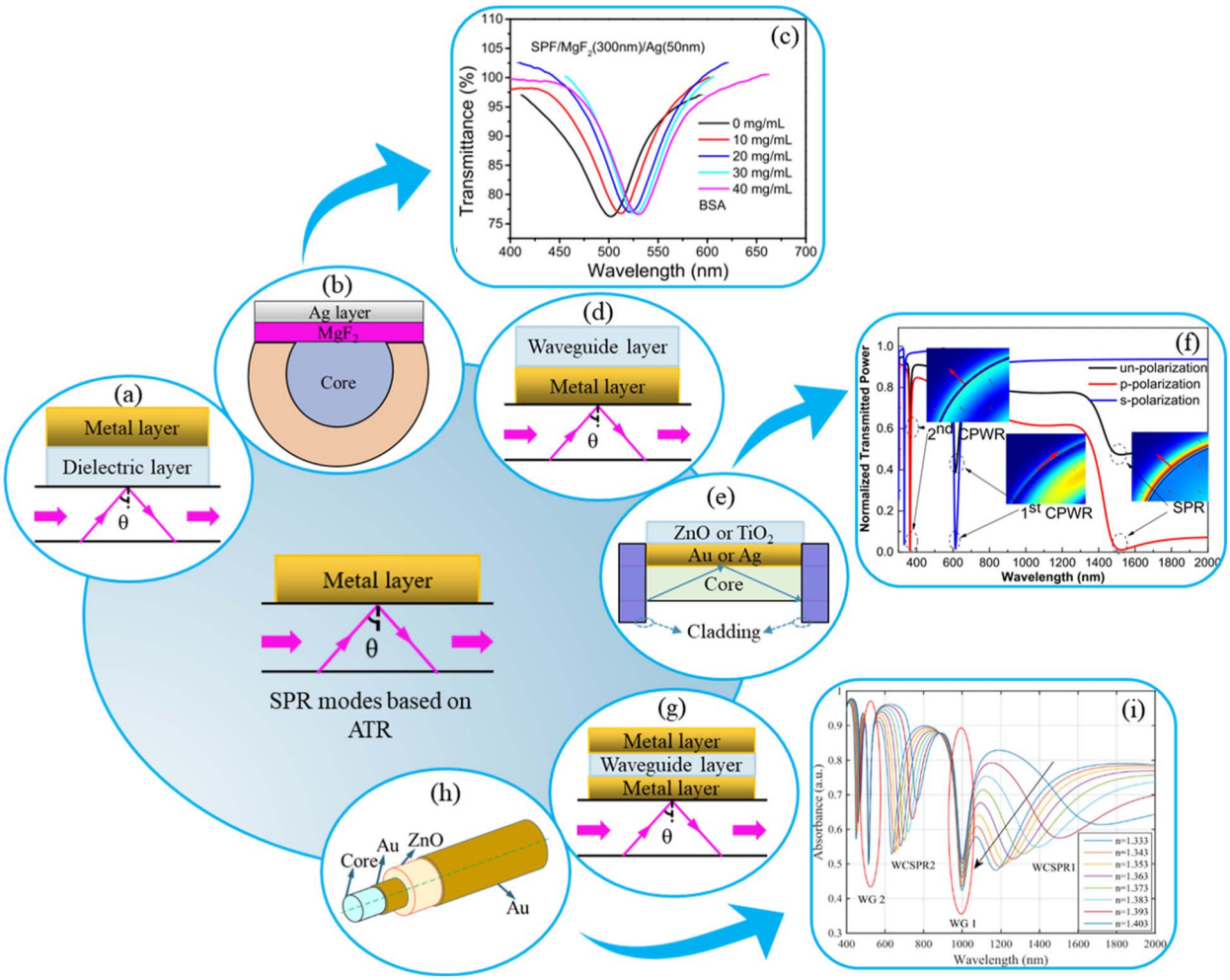

Fig. 4. (a) Layer configuration of LRSPR sensor. (b) Schematic of the sensing structure and (c) resonance spectrum for the detection of different BSA concentrations in the SPF/MgF_2/Ag-based LRSPR sensor [78]. (d) The layer configuration of CPWR sensor. (e) Schematic of the sensing structure and (f) transmission spectrum and the mode field distributions of the optical fiber CPWR sensor [80]. (g) The layer configuration of the WCSPR sensor. (h) Schematic of the sensing structure and (i) resonance spectrum for the RI detection in the optical fiber WCSPR sensor [81].

of SPPs forms a symmetrical mode, i.e., long range SPPs (LRSPPs) [43]. Its energy is mainly focused in the dielectric on both sides of the metal layer, which shows a property of low damping [82]. The penetration depth of the LRSPP's electromagnetic energy in the dielectric layer and the propagation distance at the interface between the dielectric layer and the metal layer are both an order of magnitude higher than that of traditional SPPs [6]. Therefore, the LRSPR sensor exhibits more advantages in detecting biological macromolecules. In 2019, Zhang *et al.* [78] proposed an LRSPR sensor for the BSA detection by successively evaporating the MgF_2 layer and the Ag layer on the side-polished large-core fiber surface. The specific sensing structure and experimental results are shown in Figs. 4(b) and 4(c), respectively. The FWHM of the sensor was as low as 47.8 nm, and the sensitivity reached 0.765 nm/(mg/mL). Although the LRSPR sensor has a narrower FWHM, the sensitivity of the sensor significantly relies on the symmetrical configuration [43]. This would restrict its detection range, to a certain extent, in the field of biochemical detection.

2. Coupled Plasmon Waveguide Resonance and Nearly Guided Wave SPR

The CPWR sensor incorporates a thick (typically 500 nm [11]) dielectric layer with high-complex permittivity (e.g., ITO [83], ZnO [80], TiO_2 [80]) as the waveguide layer over the traditional SPR sensor surface, as shown in Fig. 4(d). When the plane wave is incident on the waveguide layer in the TM or the transverse electric (TE) mode, the light will be both reflected and refracted at the waveguide layer interface. The resulted multiple rays will interfere due to the existence of the optical path difference, to form the waveguide resonance mode and to generate the waveguide mode resonance [43]. In 2018, Liu *et al.* [80] established a simulation model of optical fiber CPWR sensor, and the specific sensing structure is shown in Fig. 4(e). The output spectrum corresponding to the incident light with different polarization states and the mode field distributions of the CPWR mode as well as the SPR mode were simulated, as shown in Fig. 4(f). Simulation results indicated that the FWHM of the interference valley according to the sensing model, to detect the RI, was as low as 26.37 nm, and the sensitivity achieved 1360.61 nm/RIU. Due to the large distance between the analyte layer and the SPPs on the metal surface, the CPWR sensor shows a lower sensitivity than the SPR sensor, but it has a narrower FWHM leading to higher SNR and DA [11].

Similar to CPWR, NGWSPR can be stimulated by coating a thin (typically 10 nm [11]) dielectric layer with high real part of the dielectric constant (e.g., TiO_2 [84,85], ZrO_2 [11,85], PbS [86], SiO_2 [85]) on the metal layer surface. Since the thickness of the dielectric layer is insufficient to support a guided mode, this leads to the spread of SPPs along the dielectric layer, where part of the evanescent field energy is coupled to the covered materials (to be measured) [11]. In 2020, Prakashan *et al.* [85] coated the core-shell nanoparticles doped SiO_2-TiO_2-ZrO_2 ternary sol on the fiber SPR sensor, which avoided the oxidation of the Ag layer and achieved the detection of mercury with a low LOD of 10 nM.

3. Waveguide Coupled SPR

WCSPR refers to an electromagnetic resonance mode generated by coating an additional metal layer on the surface of the waveguide layer, based on CPWR. The layer configuration is shown in Fig. 4(g). When the light ray is incident at a small angle, the SPPs propagating along the interface between the lower metal layer and the waveguide layer will be excited by the TM polarized light. With the increase of the incident angle, the SPPs on the interface between the upper metal layer and the waveguide layer will also be excited [43]. Due to the coupling between the SPR and the waveguide resonance modes generated by the interference between multiple rays, narrow resonance dips and interference valleys that do not shift with the change of the external RI appear in the transmission spectrum [81]. In 2019, Ma *et al.* [81] developed a WCSPR sensor by sputtering Au-ZnO-Au layers successively on fiber core surface, and the specific sensing structure is shown in Fig. 4(h). Simulation results in Fig. 4(i) indicated that the sensor with optimal structural parameters realized the RI measurement with a sensitivity range of 2198–4732 nm/RIU, which was 7%–131% higher than that of the traditional SPR sensor. Compared with traditional SPR, the WCSPR sensor has slightly higher sensitivity and narrower FWHM, which means a higher DA. WCSPR can be regarded as a compromise between the traditional SPR and the CPWR [43].

4. Comparison of ATR-Based SPR Modes

Due to unique sensing characteristics of ATR-based SPR modes, corresponding sensors are suitable for different applications, e.g., stimulating stronger surface enhanced Raman scattering (SERS) signal for pH sensing [87] and obtaining biological information regarding the cellular micromotion [88] and the DNA hybridization [89]. Different types of ATR-based SPR modes are summarized in Table 2 for a comparison.

C. Applications of Various-Dimensionality Nanomaterials in Fiber SPR Sensing

1. Zero-Dimensional Nanomaterials

Zero-dimensional nanomaterials are confined in the nanoscale range (1–100 nm) in all three directions, and their electrons cannot move freely, e.g., nanospheres [90] and nanoparticles [91]. In 2020, Wang *et al.* [75] implemented an SPP coupled optical fiber biosensor, as shown in Fig. 5(a), for the human IgG detection. When the antigen modified on the Au nanoparticles (AuNPs) was combined with the antibody modified on the sensor surface, the near-field electron coupling, between the LSPR arising from the AuNPs and the SPR arising from the Au layer, would greatly amplify the SPR response signal. Experimental results in Fig. 5(b) indicated that the LOD of the sensor achieved as low as 0.015 μg/mL. In 2016, Shi *et al.* [92] presented a rapid method for the fabrication of the fiber SPR sensor through the polydopamine (PDA)-accelerated electroless plating (ELP), as shown in Fig. 5(c). Spherical Au seeds were at first adsorbed onto the PDA functionalized fiber surface by amino and imino intermediates generated during the polymerization, and then an Au layer was deposited. The developed sensor showed the advantages of fast fabrication and good

Table 2. Comparison of Different ATR-Based SPR Modes

ATR-Based SPR Mode	Layer Configuration	Polarization State of Excitation Light	Advantage	Disadvantage
SPR	Substrate/metal layer/analyte	TM	The layer configuration is simple, and the sensitivity is high.	The FWHM is wide, and the DA is low.
LRSPR	Substrate/dielectric layer with permittivity is pure real-number and lower than that of substrate/metal layer/analyte	TM	The FWHM is narrow, the DA is high, and the sensor is suitable for biomacromolecules detection.	The sensitivity depends heavily on symmetric configuration.
CPWR	Substrate/metal layer/thick waveguide layer with high-complex permittivity/analyte	TM or TE	The FWHM is narrow, and the DA is high.	The sensitivity is low.
NGWSPR	Substrate/metal layer/thin waveguide layer/analyte	TM	The sensitivity is high, and the resonance dip is deep.	The DA is low.
WCSPR	Substrate/metal layer/waveguide layer/metal layer/analyte	TM or TE	The sensitivity is slightly higher, and the sensor possesses self-reference function.	The layer configuration is complex.

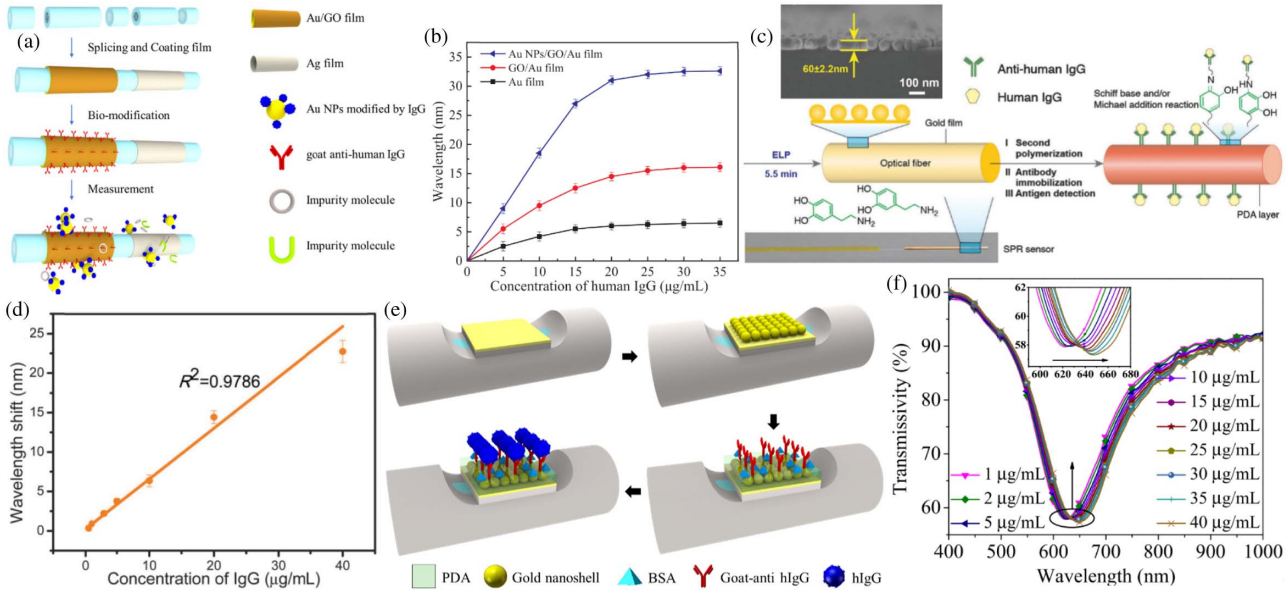

Fig. 5. (a) Fabrication process in the SPP coupling-based fiber biosensor [75]. (b) Variation of resonance wavelength for human IgG detection [75]. (c) Schematic of the fiber SPR sensor fabricated by PDA accelerated ELP for immunoassay. Inset, scanning electron microscopy (SEM) image of the Au seeds formed Au layer [92]. (d) Sensitivity fitting curve of the sensor for detecting different concentrations of human IgG [92]. (e) Fabrication process in the HGNPs modified fiber LRSPR biosensor [51]. (f) Resonance spectrum for human IgG detection [51].

stability, and realized the high-sensitivity detection for human IgG, as shown in Fig. 5(d).

Due to the assistance of the coupling between the inner and the outer walls, the hollow gold nanoparticles (HGNPs) have a stronger plasmonic field compared to solid GNPs [93]. In 2021, Cheng *et al.* [51] implemented an HGNPs modified fiber LRSPR sensor as shown in Fig. 5(e). Based on the Schiff base and Michael addition reaction between dopamine and amino or thiol-terminated biomolecules [94], the sensor utilized PDA as a coupling agent to immobilize antibodies for detecting the human IgG. The achieved LOD was 0.20 μg/mL while the FWHM of the SPR curve was wider due to the increased radiation damping caused by the light scattering of the HGNPs, as shown in Fig. 5(f). In addition, the utilization of liposome particles [95], magnetic nanoparticles (with super paramagnetic property) [91], polymer particles [96], quantum dots [97], and the further combination of them and the sandwich immunoassay, to increase the molecular weight on the sensor surface [93], can greatly improve the performance of SPR sensors.

Based on the above discussion, typical application examples of zero-dimensional nanomaterials applied in improving the SPR sensing performance are listed in Table 3.

2. One-Dimensional Nanomaterials

One-dimensional nanomaterials are confined in the nanoscale range in two directions and are extended to the macroscale range in the last direction. Their electrons can only move freely in one direction, e.g., nanotubes [38], nanorods [104], nanowires [105], and nanofibers [106]. Carbon nanotubes (CNTs) have been widely applied in the fields of biochemical sensing, nano-optics, and photothermal conversion owing to their

Table 3. Application Examples of Zero-Dimensional Nanomaterials in SPR Sensing

		Simulated/Experimental Results			
Sensing Structure	**Target Analyte**	**Sensitivity**	**LOD**	**Notes**	**Ref.**
Fiber/Au layer/AuNPs/analyte	RI 1.3332–1.3710	3074.34 nm/RIU	–	–	[98]
Fiber/Au seeds formed Au layer/PDA/anti-IgG/IgG	RI 1.333–1.359/1.359–1.386 Human IgG 2–100 μg/mL	2054/3980 nm/RIU 0.41 nm/(μg/mL)	– 0.90 μg/mL	The FOM of the sensor was 19 RIU^{-1}.	[32]
Fiber/PDA/Au seeds formed Au layer/PDA/anti-IgG/IgG	RI 1.328–1.386 Human IgG 0.5–40 μg/mL	1391–5346 nm/RIU 0.65 nm/(μg/mL)	– 0.22 μg/mL	–	[92]
Fiber/DML/Au layer/PDA-HGNPs/anti-IgG/IgG	Human IgG 1–40 μg/mL	1.84 nm/(μg/mL)	0.20 μg/mL	DML refers to dielectric matching layer. Combination of LRSPR and electric field coupling effects. The spike-and-recovery for serum samples detection was 107.62%.	[51]
Fiber/Au layer-PMBA/glucose/AuNPs-AET-PMBA	Glucose 10^4–3×10^7 nM	–	80 nM	PMBA and AET refer to p-mercaptophenylboronic acid and 2-aminoethanethiol, respectively.	[99]
PCF/Au layer/GO/anti-IgG/AuNPs-IgG	RI 1.3323–1.3359 Human IgG 1–35 μg/mL	13,592.36 nm/RIU 1.36 nm/(μg/mL)	1.47×10^{-6} RIU 0.015 μg/mL	Synergistic sensitization of zero-dimensional AuNPs and two-dimensional graphene oxide (GO).	[75]
Fiber core/Au layer/$MoSe_2$ layer/PDA/$MoSe_2$-AuNPs/PDA/IgG/anti-IgG	Goat-anti-IgG 5–25 μg/mL	7.31×10^{-3} nm/(μg/mL)	0.054 μg/mL	Synergistic sensitization of zero-dimensional AuNPs and two-dimensional $MoSe_2$.	[100]
Fiber core/Ag layer/ERY imprinted nanoparticles	ERY 10–10^5 nM	0.205 nm/nM	1.62 nM	ERY refers to erythromycin. The spike-and-recovery for real samples detection was 98.2%–102.0%.	[101]
Fiber/Ag core-SiO_2 shell-AuNPs/analyte	γ-aminobutyric acid 10^{-9} – 10^6 nM	2 nm/lg[M]	1.65×10^{-6} nM	The LOD for serum samples was 1.88×10^{-14} M.	[90]
Fiber/triangular AgNPs/GO/analyte	RI 1.3318–1.3495	1114.80 nm/RIU	–	The apices generated greater electric field amplification.	[102]
Fiber/Au nanostars arrays	SERS	–	–	The apices generated greater electric field amplification, and the proposed sensor was demonstrated with 45 times electric field intensity enhancement compared with Au nanorods design.	[103]

extraordinary chemical, electrical, and optical characteristics. In 2021, Pathak *et al.* [38] embedded palladium nanoparticles (PdNPs) in polypyrrole (ppy) coated MWCNTs and established a fiber optic SPR sensing system, as shown in Fig. 6(a), for the hydrazine detection. CNTs have a high RI, which makes it easier for the evanescent field energy to be coupled into the outer space of the metal layer. This thereby enhanced the light-matter interaction and promoted the perception capability of the sensor to the ambient environment changes [107]. The electronegativity of the CNT's surface promoted the transfer of electrons from CNTs to the Au layer surface and thereby strengthened the electric field intensity on the surface of the sensing region [38]. The superposition of the electric field stimulated by adjacent CNTs further strengthened the confined electric field on the sensor surface. Moreover, the CNT's modified sensor surface can absorb more molecules than the bare Au layer due to the large specific surface area and the excellent biocompatibility of CNTs [108]. Therefore, experimental results in Fig. 6(b) indicated that the LOD was as low as 20 nM.

The modification of Au nanorods on the surface of SPR sensor can effectively enhance the sensitivity of the sensor because of the transverse and the longitudinal plasmon electric field coupling between nanorods and the Au layer [91]. In 2020, Xia *et al.* [104] developed a multilayer Au nanorod modified PCF-SPR sensor, as shown in Fig. 6(c). The sensitivity of the sensor in detecting the RI, for the range of low-concentration biological solutions, can achieve up to 25,642.65 nm/RIU. Experimental results in the detection of human IgG solutions with different concentrations are shown in Fig. 6(d), which indicated that the LOD was as low as 4.6 ng/mL. If the Au nanorods form an array structure and the distance between nanorods is smaller than the wavelength, the formed metamaterials layer supports a guided mode with the field distribution decided by the plasma-mediated interaction between nanorods [109]. Based on the overlap between the detection field, bioactive substances in metamaterial layer, and the confined plasma-mediated energy, the sensitivity of the sensor will be greatly enhanced [109]. Similarly, Kant *et al.* [106] employed an electrospinning setup for the synthesis of xanthine oxidase (XO) entrapped Ta_2O_5 nanofibers and modified them on the surface of the fiber SPR sensor, as shown in Fig. 6(e) for the xanthine detection. Experimental results in Fig. 6(f) indicated that the sensor had a high sensitivity and the LOD was as low as 12.70 nM.

Based on the above discussion, typical application examples of one-dimensional nanomaterials applied in improving the SPR sensing performance are listed in Table 4.

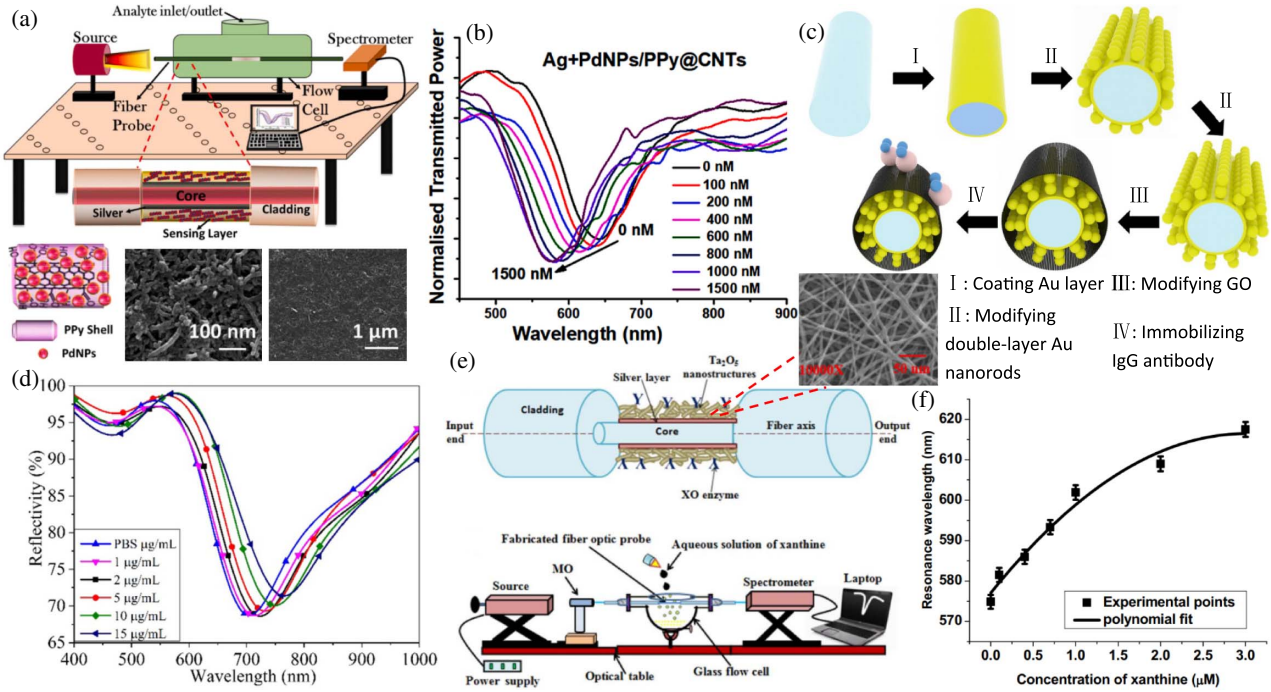

Fig. 6. (a) Schematic of the PdNPs embedded/PPy shell coated MWCNT-based fiber SPR probe and the laboratorial setup. Inset, schematic and SEM image of the PdNP embedded/PPy shell coated MWCNTs and SEM image of the fiber probe surface [38]. (b) Resonance spectrum obtained by detecting hydrazine with different concentrations [38]. (c) The fabrication process of the double-layer Au nanorods and GO sensitized PCF-SPR sensor [104]. (d) Resonance spectrum obtained by detecting human IgG with different concentrations [104]. (e) Schematic of the Ta_2O_5 nanofiber sensitized fiber SPR probe and the laboratorial setup. Inset, SEM image of the synthesized Ta_2O_5 nanofibers [106]. (f) Variation of resonance wavelength for xanthine detection [106].

3. Two-Dimensional Nanomaterials

Two-dimensional nanomaterials are confined in the nanoscale range in one direction and are expanded to the macroscale range in other two directions. Their electrons can only move freely in such two directions. Two-dimensional nanomaterials popularly used for improving the performance of SPR sensors are listed in Table 5. Graphene possesses lower energy losses (e.g., Ohmic loss and radiative loss), high electron transport mobility, and high surface-to-volume ratio, and it can accommodate more organic and biological molecules because of the π stacking interaction between the carbon-based ring structure of molecules and hexagonal cells of graphene [122]. The position of each graphene atom can be involved in the interaction between biomolecules, which means that graphene may eventually realize the single-molecule detection. GO has a hexagonal carbon structure similar to graphene and also contains the oxygen functional group such as hydroxyl, alkoxy, and carboxyl. This results in its higher solubility and easier surface functionalization for various types of biological receptors [122]. Phosphorene has also been applied in photonic sensor research works due to its high carrier mobility, strong carrier confinement, tunable direct bandgap, and anisotropic electron and photon characteristics [123,124]. The high carrier mobility and light absorption of TMDCs enable the effective use of light energy in the electron transmission. This leads to a strong coupling on the interface, thereby will enhance the surface energy density of the sensing layer and will amplify the response of the sensor to the RI disturbance in the sensitive layer [125].

Different two-dimensional layered materials can be vertically stacked together and integrated to form van der Waals heterostructures and superlattices. This can manipulate optical and electronic characteristics of their interlayer interactions, to provide technical support for the development of next-generation devices [126]. In 2019, Rahman *et al.* [127] theoretically designed a phosphorene-graphene/TMDC heterostructure-based fiber SPR biosensor, as shown in Fig. 7(a). BP improved the sensing performance by amplifying the interlayer coupling of van der Waals forces [130]. The stacking of the layered structure allows the thickness to be precisely controlled and the avoidance of the metal oxidation. Meanwhile, the sensitivity of the sensor can be controlled by the number of layers in the two-dimensional nonomaterials. The proposed biosensor also exhibited vast application potential in the DNA detection, as shown in Fig. 7(b).

MXene can realize the attractive biosensing due to its chemical stability, fully functionalized surface termination, high metal conductivity, tunable direct bandgap, small work function, large adsorption energy, and hydrophilic biocompatible surface [123,126,131]. In 2020, Chen *et al.* [128] developed a $Ti_3C_2T_x$ MXene improved fiber SPR sensor [in Fig. 7(c)] for the RI detection. Experimental results in Fig. 7(d) demonstrated that, for the first time, characteristics of $Ti_3C_2T_x$ MXene could enhance the sensitivity of fiber biosensors. The modification of some perovskite materials with high RI and low dielectric loss on the SPR sensor surface to stimulate NGWSPR can also strengthen the intensity of the evanescent electromagnetic field on the

Table 4. Application Examples of One-Dimensional Nanomaterials in SPR Sensing

Sensing Structure	Target Analyte	Simulated/Experimental Results			Notes	Ref.
		Sensitivity	FOM	LOD		
Fiber core/ITO/Si/SWCNTs/analyte	RI 1.330–1.335	9780 nm/RIU	9.76 RIU^{-1}	–	ITO and SWCNTs refer to indium tin oxide and singlewalled CNTs, respectively.	[83]
Fiber core/Au layer/MWCNTs-PtNPs/analyte	RI 1.3385–1.3585	5923.14 nm/RIU	29.32 RIU^{-1}	–	Synergistic sensitization of zero-dimensional platinum nanoparticles (PtNPs) and one-dimensional MWCNTs.	[108]
Fiber/Au layer/MWCNTs-CuNPs/analyte	Nitrate 2.5×10^3–10^6 nM	3.25 nm/lg[M]	–	–	Simultaneous measurement of two parameters. Synergistic sensitization of zero-dimensional cuprum nanoparticles (CuNPs) and one-dimensional MWCNTs.	[110]
	Temperature	−2.02 nm/°C	–	–		
Fiber core/Ag layer/MWCNTs-CuNPs/analyte	Nitrate 10^3–5×10^6 nM	0.08062 nm/nM	–	4 nM	Synergistic sensitization of zero-dimensional CuNPs and one-dimensional MWCNTs.	[107]
Fiber core/Ag layer/PdNPs-PPy-MWCNTs/analyte	Hydrazine 0–1.5×10^3 nM	0.09 nm/nM	–	20 nM	Synergistic sensitization of zero-dimensional PdNPs and one-dimensional MWCNTs. The spike-and-recovery rate of real sample detection was 97.5%–102.8%.	[38]
Fiber core/Ag layer/MWCNTs/analyte	Sulfamethaxazole 0–2×10^5 nM	0.37×10^{-3} nm/nM	–	891.80 nM	–	[111]
Fiber core/Ag layer/PPy-MWCNTs/analyte	Dopamine 0–10^4 nM	68.58 nm/lg[M]	–	0.0189 nM	–	[112]
Fiber core/Ag layer/graphene-MWCNTs-poly-(methyl methacrylate)/analyte	Methane gas 10–100 ppm (parts per million)	–	–	–	Synergistic sensitization of one-dimensional MWCNTs and two-dimensional graphene. The maximum shift in the resonance wavelength was 30 nm for methane gas detection.	[113]
Fiber core/Ag layer/Ta_2O_5 nanofibers/XO enzyme/analyte	Xanthine 0–3×10^3 nM	0.0262 nm/nM	–	12.70 nM	The sensor worked well for the detection of xanthine in green tea samples.	[106]
Fiber core/Ag layer/ZnO: graphene nanofibers/analyte	Nicotine 0–10^4 nM	4.50×10^{-3} nm/nM	–	74 nM	The sensor worked well for the detection of nicotine in cigarette samples.	[114]
PCF/Au layer/Au nanorods/GO/Au nanorods/analyte	RI 1.3323–1.3361	22,248.22 nm/RIU	–	8.99×10^{-7} RIU	Synergistic sensitization of one-dimensional Au nanorods and two-dimensional GO.	[115]
	Human IgG 1–15 μg/mL	3.28 nm/(μg/mL)	–	6.10 ng/mL		
PCF/Au layer/double-layer Au nanorods/GO/analyte	RI 1.3320–1.3366	25,642.65 nm/RIU	–	7.80×10^{-7} RIU	Synergistic sensitization of one-dimensional Au nanorods and two-dimensional GO.	[104]
	Human IgG 1–15 μg/mL	4.35 nm/(μg/mL)	–	4.60 ng/mL		
U-bent fiber/Au layer/ITO nanorods/graphene/analyte	RI 1.3330–1.3634	690.70 nm/RIU	–	–	Synergistic sensitization of one-dimensional ITO nanorods and two-dimensional graphene.	[116]
	DNA 0.1–100 nM	–	–	0.10 nM		
PCF/Ag nanowires/analyte	RI 1.33–1.38	9314.28 nm/RIU	1494 RIU^{-1}	1.073×10^{-5} RIU	–	[117]
PCF/Au nanowires/analyte	RI 1.32–1.38	10,286 nm/RIU	146.90 RIU^{-1}	9.72×10^{-6} RIU	–	[118]
Fiber/bimetallic nanowire gratings/analyte	RI 1.33–1.49	643.75 nm/RIU	–	–	–	[105]

sensing layer surface [129,132,133]. In 2020, Xia *et al.* [129] successively coated Au layer and ferroelectric crystal-$BaTiO_3$ on the polymer-tipped optical fiber (PTOF), as shown in Fig. 7(e), and experimental results in Fig. 7(f) indicated the improvement of the performance of the SPR sensor.

Based on the above discussion, typical application examples of two-dimensional nanomaterials applied in improving the SPR sensing performance are listed in Table 6.

4. Three-Dimensional Nanomaterials

Three-dimensional nanomaterials represent composites composed of one or more basic structural units from zero-dimensional, one-dimensional, and two-dimensional materials, e.g., three-dimensional superlattice structures [146,147] and nanostructured metal architectures [148,149].

In 2020, Li *et al.* [150] implemented a U-shaped MMF LSPR biosensor based on the three-dimensional hyperbolic

Table 5. Popular Two-Dimensional Materials for SPR Sensor Performance Improvement

Category	Basic Chemical Formula	Ensample
Graphene and derivatives	–	GO, reduced GO (rGO)
Phosphorene	–	Black phosphorus (BP), BlueP
Transition metal dichalcogenides (TMDCs)	MX_2	HfS_2, VSe_2, $MoTe_2$
MXene	M_2Y, M_3Y_2, or M_4Y_3	$Ti_3C_2T_x$
Perovskite	ZMO_3	$BaTiO_3$, $CaTiO_3$
Notes	M, X, Y, Z, and T_x represent transition metal element, chalcogen, carbon or nitrogen, alkaline-earth elements, and surface functionalities such as -O, -F, or -OH, respectively [119–121].	

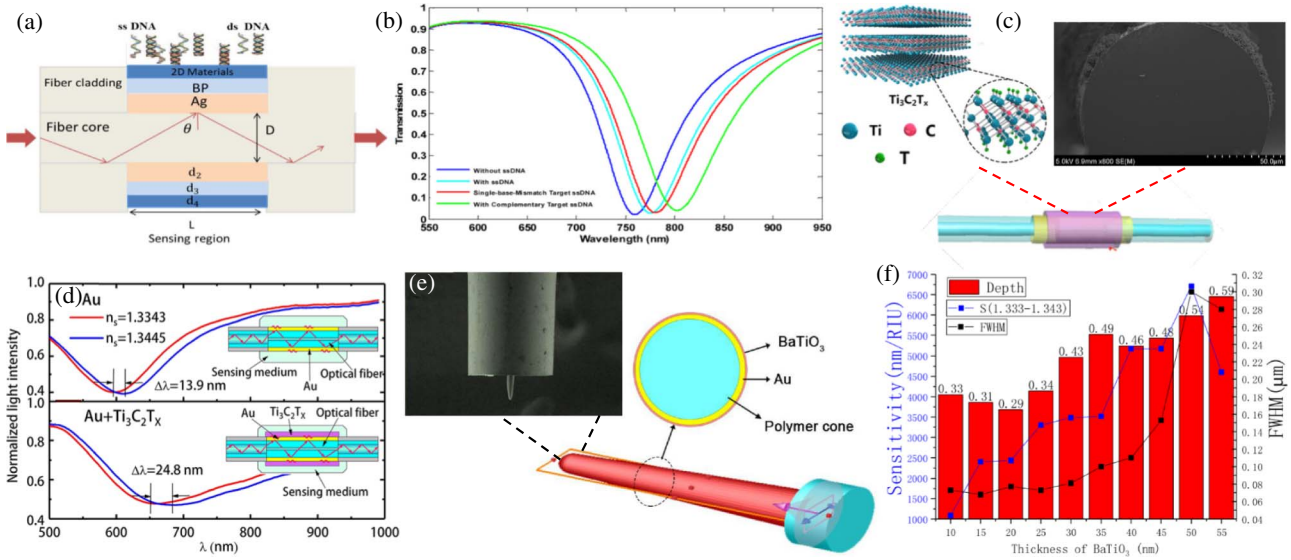

Fig. 7. (a) Schematic of the phosphorene-graphene/TMDC heterostructure-based fiber SPR biosensor [127]. (b) Resonance spectrum of the biosensor for DNA hybridization detection [127]. (c) Schematic of the $Ti_3C_2T_x$ MXene improved fiber RI sensor and SEM image of the cross section of the sensor [128]. (d) Transmittance versus wavelength for the sensor without and with $Ti_3C_2T_x$ MXene [128]. (e) Three-dimensional model of the PTOF coated with $BaTiO_3$ layer and SEM image of the sensor [129]. (f) Sensitivity and FWHM of the sensor with different thicknesses of $BaTiO_3$ layer [129].

super-material structure of multilayer graphene coated Au nanoparticles. The fabrication procedure of the biosensor is shown in Fig. 8(a). In Fig. 8(b), the multilayered structure formed by the repeated synthetization of the nanoparticle layer and the graphene enhanced the vertical charge density oscillation and transformed the plasma oscillation mode from a planar structure to a three-dimensional structure. This led to a strong LSPR effect. It was found in Fig. 8(c) that this biosensor displayed excellent performance in the DNA hybridization kinetics measurement. In 2018, Daems *et al.* [151] designed three types of three-dimensional DNA origamis as bioreceptor carriers to functionalize the fiber SPR sensor for the detection of thrombin, as shown in Fig. 8(d). The produced biosensor showed the better performance in the absence of backfilling and a wider linear range. Experimental results in Fig. 8(e) indicated that the LOD was as low as 6.1 nM.

Based on the quantum size effect, the surface effect, and the dielectric confinement effect, nanomaterials with new functions are expected if there are further breakthroughs in the structure, the composition, the arrangement, and the size of three-dimensional nanomaterials.

4. FUTURE DIRECTIONS OF DEVELOPMENT

A. End-Face Reflective Sensing Structure

Compared with the transmission-type optical fiber SPR sensor [152] shown in Fig. 9(a), the end-face reflective optical fiber SPR sensor can be inserted into a small piece of sample or cramped space to directly acquire the signal in the dip-and-read way. Combined with mature fiber communication technology, this can achieve the high-efficiency, low-damage, and invasive measurement. At present, there are mainly three types of end-face reflective fiber SPR sensing probes [14], as shown in Fig. 9(a). On the cylindrical surface at the end of fiber, the cladding is removed, and a metal layer is coated to stimulate the SPR. Meanwhile, the end-face of fiber is also coated with the metal to serve as a mirror. Moreover, when the light is reflected from the end-face and enters the fiber again, the optical path is doubled, which enhances the plasmon resonance effect. In 2019, Kong *et al.* [153] fabricated a SiO_2-microtip probe on the SMF end-face based on arc discharge technology. The probe surface was coated with an Au layer and was connected to the laboratorial testbed in Fig. 9(b) to realize the

Table 6. Application Examples of Two-Dimensional Nanomaterials in SPR Sensing

		Simulated/Experimental Results				
Sensing Structure	**Target Analyte**	**Sensitivity**	**FOM**	**LOD**	**Notes**	**Ref.**
Fiber core/Ag layer/Pt layer/ITO/graphene/analyte	RI 1.33–1.36	4150 nm/RIU	70 RIU^{-1}	–	–	[134]
Fiber core/Ag layer/GO/analyte	Glucose adulterant	21,140 nm/RIU	–	2.33×10^{-5} RIU	–	[135]
	Fructose adulterant	18,890 nm/RIU	–	1.53×10^{-4} RIU		
Fiber core/Ag layer/Au layer/MoS_2/analyte	RI 1.3318–1.3701	3061.84 nm/RIU	23.29 RIU^{-1}	–	–	[136]
Fiber core/Au layer/MoS_2/anti-BSA/BSA	BSA 10–50 μg/mL	0.9234 nm/(μg/mL)	–	0.29 μg/mL	–	[137]
Fiber/MoS_2/Au layer/analyte	RI 1.3314–1.3623	6184.40 nm/RIU	–	3.23×10^{-6} RIU	–	[125]
	Human IgG 5–70 μg/mL	1.014 nm/(μg/mL)	–	1.97×10^{-2} μg/mL		
Fiber core/Cr layer/Au layer/$MoSe_2$/analyte	RI 1.333–1.358	2793.36 nm/RIU	37.24 RIU^{-1}	–	–	[138]
	Goat-anti-rabbit IgG $10–10^3$ μg/mL	–	–	0.33 μg/mL		
Fiber core/Al layer/graphene/MoS_2/analyte	RI 1.330–1.332	6200 nm/RIU	–	–	–	[139]
SPF/Cr layer/Au layer/MoS_2/graphene/PBA/analyte	Glucose $0–3 \times 10^3$ μg/mL	6708.87 nm/RIU	–	–	PBA refers to pyrene-1-boronic acid.	[4]
Fiber core/Au layer/BP/2-D materials/analyte	Graphene	4050 nm/RIU	39.70 RIU^{-1}	–	2-D materials refer to two-dimensional materials. The sensor was also utilized successfully to detect DNA hybridization.	[127]
	MoS_2	RI 1.33–1.39	3950 nm/RIU	40.25 RIU^{-1}	–	
	$MoSe_2$		3975 nm/RIU	41.40 RIU^{-1}	–	
	WS_2		3975 nm/RIU	47.89 RIU^{-1}	–	
	WSe_2		4000 nm/RIU	47.62 RIU^{-1}	–	
Fiber core/NaF layer/Ag layer/BlueP/2-D materials/analyte	MoS_2	D_2O/H_2O	–	15,650.75 RIU^{-1}	–	[140]
	WS_2		–	12,409.30 RIU^{-1}	–	
Fiber core/Ag layer/SnSe/analyte	RI 1.33–1.37	3475 nm/RIU	–	–	–	[141]
Fiber core/Ag layer/GNP-SnO_2/analyte	Dopamine 0–100 μM	10.66 nm/μM	–	0.031 μM	GNP refers to graphene nanoplatelet.	[142]
Fiber core/Ag layer/Ta_2O_5 nanoflakes/analyte	Acetylcholine 0–10 μM	8.709 nm/μM	–	0.038 μM	–	[143]
Heterocore fiber/Au layer/$Ti_3C_2T_x$ MXene/analyte	RI 1.3343–1.3658	2180.20 nm/RIU	–	–	–	[128]
Fiber core/Au layer/Ti_3C_2 MXene/analyte	RI 1.333–1.335	3725 nm/RIU	48.28 RIU^{-1}	–	–	[144]
PTOF/Au layer/$BaTiO_3$/analyte	RI 1.333–1.343	6710 nm/RIU	–	–	–	[129]
SPF/Au layer/$BaTiO_3$/analyte	RI 1.3332–1.3710	2543.33 nm/RIU	–	–	–	[145]
	RI 1.3710–1.4140	6040.42 nm/RIU	–	–		

biochemical detection at a single-cell level. A bio-probe was produced in Fig. 9(c) by immobilizing the antibody on the Au layer surface via a nano-polyelectrolyte film of chitosan/polysodium styrene sulfonate (Cs/PSS), and it was utilized for the human IgG detection. Experimental results in Figs. 9(d) and 9(e) indicated that the sensitivity and the LOD of the bio-probe reached 0.19154 nm/(ng/mL) and 0.1 ng/mL, respectively.

B. Combination of Nanoarray Structure and Fiber SPR Sensing

A highly ordered plasmonic nanoarrays, produced by self-assembly technology [154], focused ion/electron beam lithography [155], and two-photon laser direct writing [37], can stimulate various coupling optical effects such as Fano resonance [156], guided mode resonance [157], surface lattice resonance (SLR) [158], and SERS [154]. The combination of

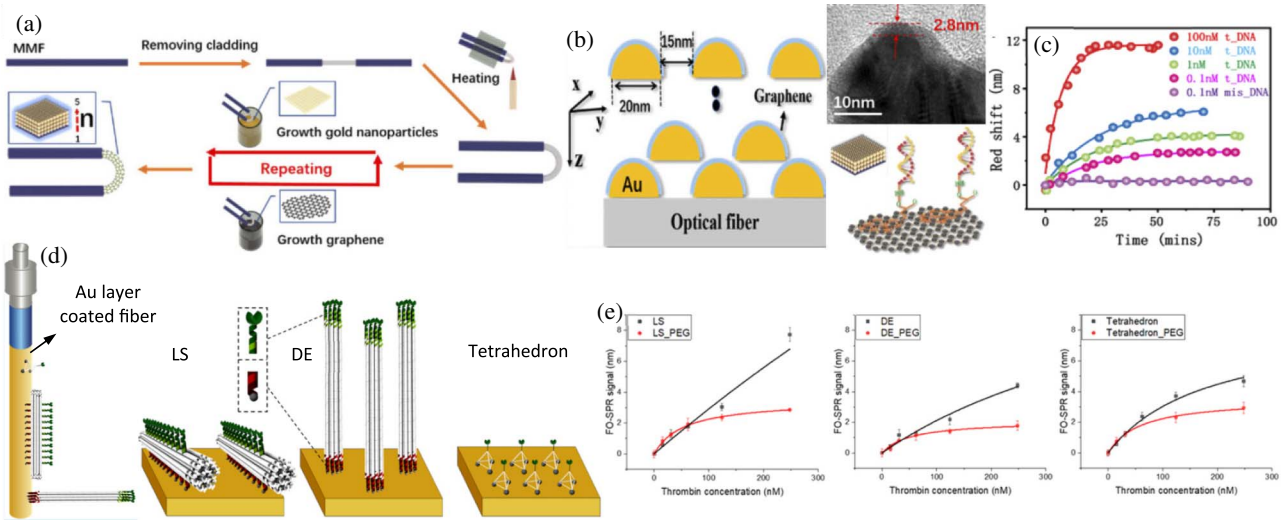

Fig. 8. (a) Preparation procedure of the three-dimensional composite-based fiber LSPR biosensor [150]. (b) Schematic of the three-dimensional composite on the fiber surface, transmission electron microscopy image of Au nanoparticles covered by multilayer graphene, and schematic of the DNA detection process [150]. (c) Real-time wavelength redshift for DNA detection [150]. (d) Schematic of the bioreceptor patterning onto the Au coated fiber surface using DNA nanotechnology: three-dimensional DNA lateral surface (LS) origami, distal ends (DE) origami, and tetrahedron. (Dark green, bioreceptors; dark gray spheres, thiol groups; light green and red, ssDNA [151].) (e) Calibration curves for thrombin bioassay on the fiber SPR biosensing platform [151].

above effects and the SPR sensing can further strengthen the light-matter interaction, can reduce the radiative loss, and can thus improve the sensor performance. The periodic nanoarray also provides tunable structure parameters, wider spectral range, and higher degree of freedom. The SPR sensor based on the nanoarray has higher sensitivity and FOM, which expands the application scenarios of SPR. Furthermore, it is compatible with existing imaging equipment, microfluidic chips, and

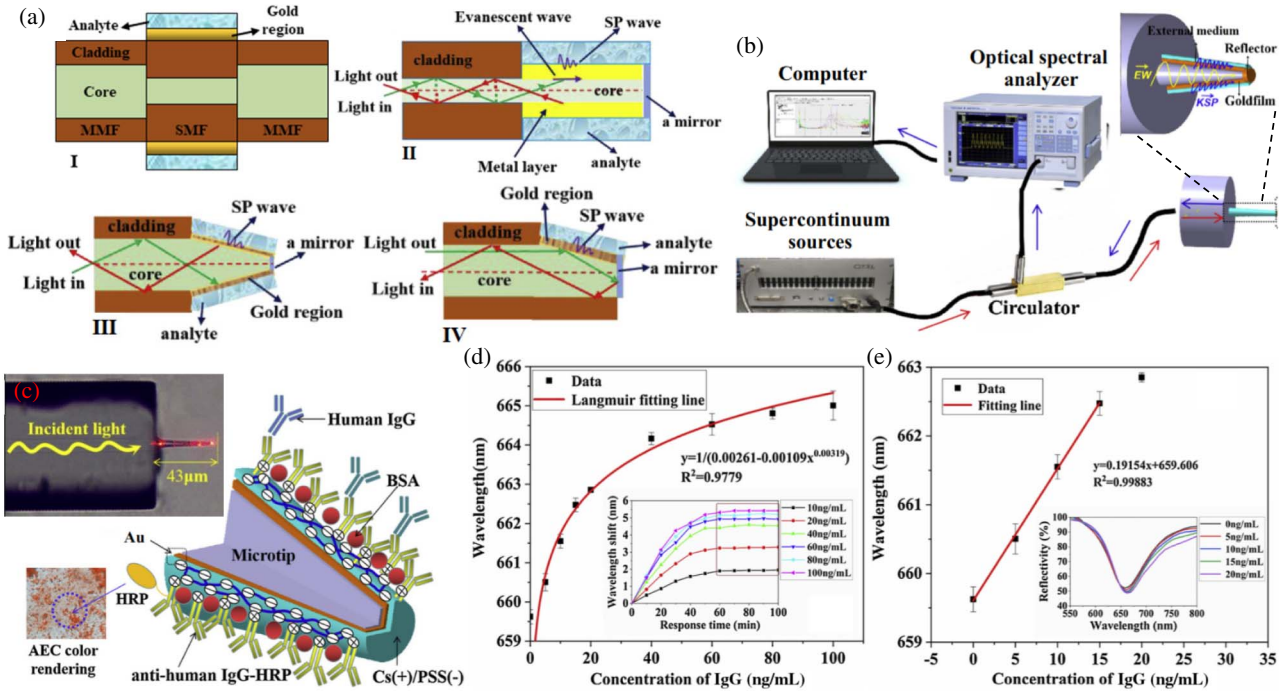

Fig. 9. (a) Transmission-type fiber SPR sensor [152] based on core mismatch I and reflective fiber SPR sensor [14] based on flat tip II, tapered tip III, and angle polished tip IV. (b) Schematic of the sensing structure of the protruding-shaped fiber plasmonic microtip probe and the testbed [153]. (c) SEM image of the microtip probe and schematic of the bio-probe [153]. (d) Langmuir adsorption curve and (e) sensitivity fitting line for human IgG detection with different concentrations [153].

photonic circuits so that the fabricated devices can be highly integrated and miniaturized. Based on the above advantages [157], nanoarray structures have attracted more and more attention.

In 2016, He *et al.* [159] implemented an SPR device on the SMF end-face, as shown in Fig. 10(a). The end-face of the fiber was first coated with a 50 nm Au layer, and then the Au layer was engraved with a square nanoslot array as illustrated in the shadow area on the Au layer. The first-order spatial Fourier component of the nanoslot array was grating coupled with the fiber-guided wave. The second-order spatial Fourier component restricted the SPP transmission and can thereby form a plasmonic crystal cavity. Such a plasmonic crystal cavity on the SMF end-face was utilized to detect the RI, and experimental results in Fig. 10(b) manifested an FOM of 68 RIU^{-1}. Based on the coupling between the SPR within a dense metal layer and multiple resonance modes stimulated locally within anisotropically shaped nanostructures [160], the plasmonic nanoarray can also be utilized to enhance the sensitivity of the traditional reflective fiber SPR sensor. In 2017, Antohe *et al.* [160] deposited nanotriangular arrays on the Au layer coated reflective fiber end-face, as shown in Fig. 10(c), and achieved an increment of 25% in the sensitivity according to Fig. 10(d).

In 2018, Wang *et al.* [161] lithographed nanotrimer arrays at the fiber end-face, as shown in Fig. 10(e), which was, for the first time, the excitation of the SLR phenomenon on the optical fiber sensor. SLR originates from the coupling of the diffracted light propagating along the array plane and the localized surface plasmons [157]. It was found that the FWHM of the SLR-based sensor, shown in Fig. 10(f), was 89.23% lower than that of the LSPR-based sensor, shown in Fig. 10(g). The FOM was increased by approximately 10 times [158].

C. Plasmonic Antenna Integrated on Tapered Fiber Tip

Lab on tip based probe devices provide high-precision dynamic tuning of plasmonic antenna and high-resolution detection through the strong interaction between plasmonic hotspots and samples. The test objects include the molecular adsorption or deformation [162], molecular vibration spectrum [163], quantum tunneling [164,165], etc.

As shown in Figs. 11(a) and 11(b), the coupling between the tapered fiber (or dielectric waveguide) and metal nanowires (or SPP waveguide) can greatly improve the light wave coupling and sub-wavelength focusing efficiency of the near-field optical microscope probe. This realized the scanning Raman spectroscopy imaging with a spatial resolution of 1 nm [166,169]. As shown in Fig. 11(c), it was observed by Danckwerts *et al.* that a sharp increase in the four-wave-mixing produced signal would occur when the Au nanoparticle-fiber probe approached another Au nanoparticle [167]. Due to the quantum tunneling effect, a sudden change of the increase trend occurred when the gap became very small. The Au nanoparticle-fiber probe was also employed to approach a single molecule. As shown in Fig. 11(d), the molecular fluorescence experienced the process of from enhancement to quenching when the probe approached a single molecule [168]. This indicated that the dynamically tuned plasmonic antenna was more conducive to the characterization of the light-matter interaction in the plasmonic hotspot.

D. Initial Conceptions

Although the fiber SPR sensors can realize the detection of physical and biochemical parameters, there is still some space to improve fiber SPR sensors in terms of accuracy, cross-sensitivities, selectivity, costs, and reliability. In the future research, it will be promising to involve microelectromechanical

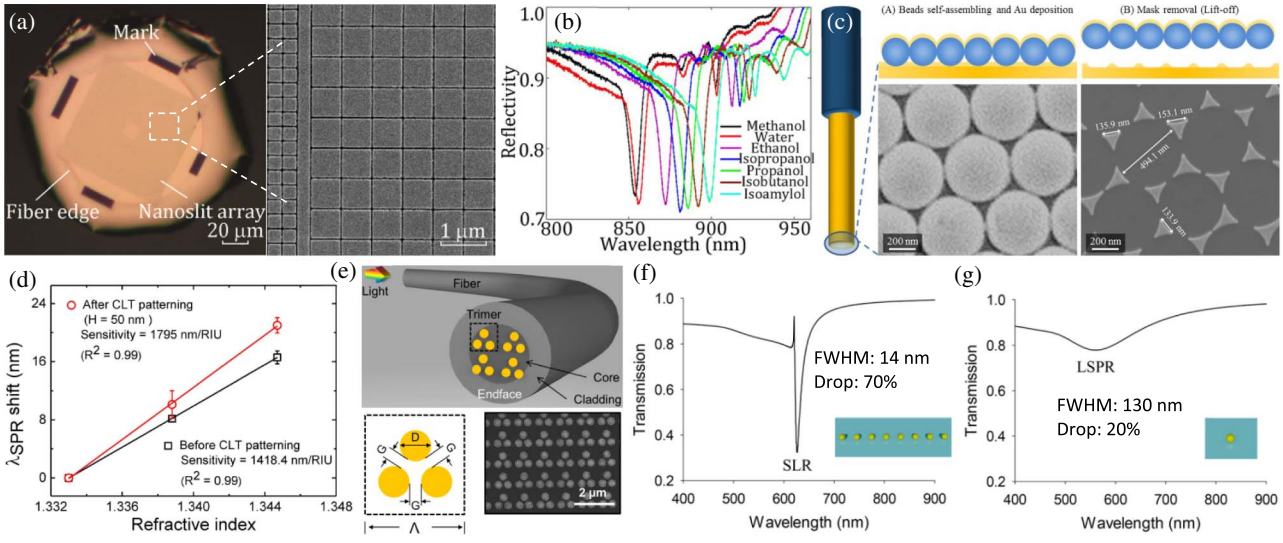

Fig. 10. (a) Optical micrograph of the plasmonic crystal cavity on the SMF end-face [159]. (b) Resonance spectrum of the SPR device for the detection of different solutions [159]. (c) Process in the fabrication of nanotriangular arrays on the reflective fiber SPR sensor end-face based on colloidal lithography technology and the SEM image of the nanotriangular arrays [160]. (d) Sensitivity fitting lines for the RI detection of the Au triangularly patterned and non-patterned sensors [160]. (e) Block diagram of the nanotrimer arrays on the bent fiber end-face and the SEM image of the nanotrimer arrays [161]. Resonance spectra of the (f) SLR-based and (g) LSPR-based sensors [158].

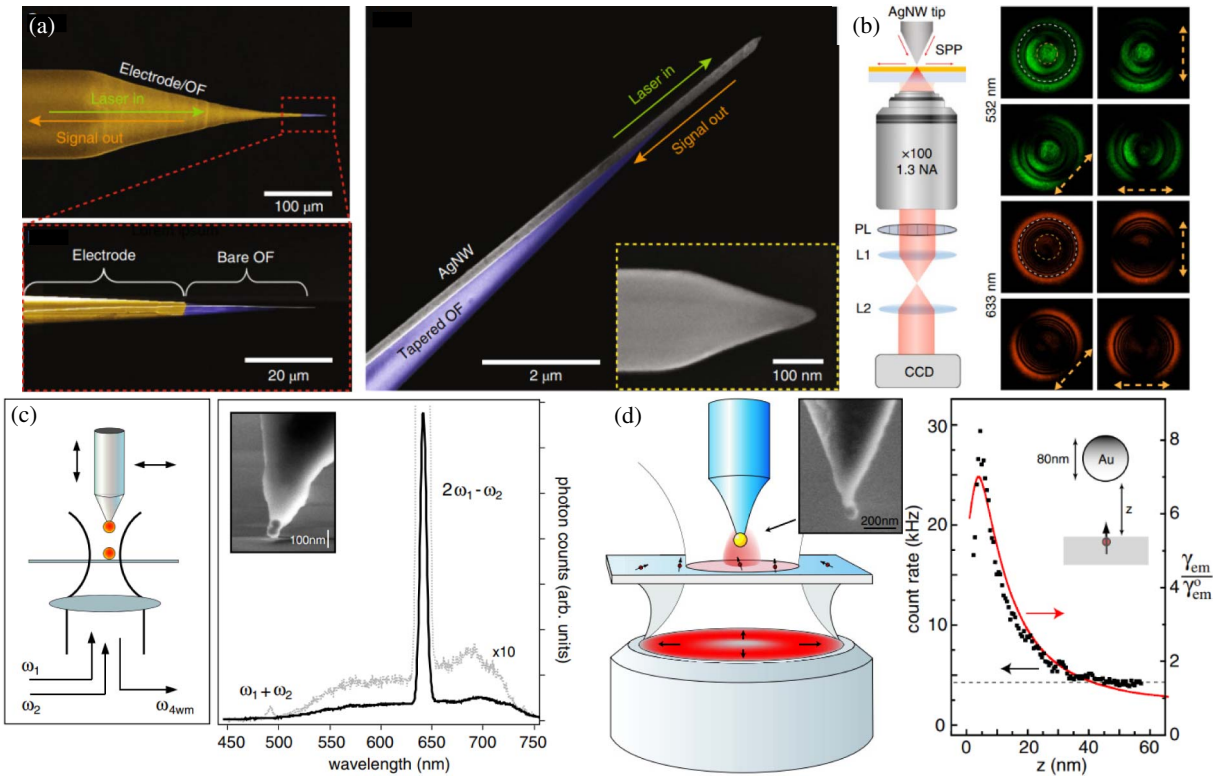

Fig. 11. (a) Near-field optical microscope probe based on the high-efficiency coupling of Ag nanowires and tapered optical fiber (AgNW-OF) [166]. (b) Polarization-resolved k-space imaging of the light emitted from the nanofocused SPP mode at the AgNW-OF probe tip [166]. (c) The four-wave-mixing produced signal increased sharply when the Au nanoparticle-fiber probe approached another Au nanoparticle [167]. (d) The molecular fluorescence changed from enhancement to quenching when the Au nanoparticle-fiber probe approached a single molecule [168].

systems [170,171] for improving the stability of the device and to employ liquid metals [172] for developing flexible optical devices. The integrated and miniaturized design of fiber SPR sensors can utilize the two-photon three-dimensional micro/nano film printing to achieve the accurate, real-time, and on-site detection [171,173]. Terahertz biosensors based on metamaterials can also be vigorously developed to achieve the non-invasive detection for biomarkers or biochemical indicators in living organisms [156,173]. According to the sensing characteristics of fiber SPR sensors modified by different nanomaterials, nanomaterials can be reversely designed at the atomic level to modify sensors to obtain desired sensing characteristics, e.g., to locate the resonance valley in the optical band. In order to improve the performance of fiber SPR sensors from different aspects, various approaches can be jointly applied in the implementation of sensors. For example, the modification of nanomaterials on the surface of the LRSPR sensor with improved metal layer quality can enhance the sensitivity of the sensor while ensuring the DA [174,175].

5. CONCLUSION

This review work summarized current major approaches for improving the performance of fiber SPR sensing and the applications of the manufactured sensors mainly in the field of biochemical detection. The sensing principle and the performance indicators including determinants of SPR sensors were demonstrated to clarify the research direction of the performance improvement. The application examples and the internal mechanisms in the SPR sensing performance improvement were reviewed from three aspects, corresponding to the basic layer configuration of fiber SPR sensors, namely substrate, intrinsic layer, and surface nanomaterial modification. Relevant contents were summarized and compared in detail. In general, the performance improvement of fiber SPR sensors mainly lies in heightening the overlap integral of the SPP electric field intensity on the sensor surface to enhance the sensitivity, reducing the energy losses of SPP to narrow down the FWHM of SPR curve and to improve the DA and the SNR, and introducing the sensing self-compensation to enhance the detection reliability. Furthermore, the development direction of fiber SPR sensors was discussed based on the state of the art in plasmonic detection technologies.

Funding. National Natural Science Foundation of China (61735011, 61775161, 61922061); Science Fund for Distinguished Young Scholars of Tianjin (19JCJQJC61400); National Equipment Program of China (2013YQ030915).

Disclosures. The authors declare no conflicts of interest.

Data Availability. Data underlying the results presented in this paper are not publicly available at this time but may be obtained from the authors upon reasonable request.

REFERENCES

1. A. Jebelli, F. Oroojalian, F. Fathi, A. Mokhtarzadeh, and M. de la Guardia, "Recent advances in surface plasmon resonance biosensors for microRNAs detection," Biosens. Bioelectron. **169**, 112599 (2020).
2. A. Koponen, E. Kerkela, T. Rojalin, E. Lazaro-Ibanez, T. Suutari, H. O. Saari, P. Siljander, M. Yliperttula, S. Laitinen, and T. Viitala, "Label-free characterization and real-time monitoring of cell uptake of extracellular vesicles," Biosens. Bioelectron. **168**, 112510 (2020).
3. G. Y. Wang, Y. Lu, L. C. Duan, and J. Q. Yao, "A refractive index sensor based on PCF with ultra-wide detection range," IEEE J. Sel. Top. Quantum Electron. **27**, 5600108 (2021).
4. H. X. Yu, Y. Chong, P. H. Zhang, J. M. Ma, and D. C. Li, "A D-shaped fiber SPR sensor with a composite nanostructure of MoS_2-graphene for glucose detection," Talanta **219**, 121324 (2020).
5. W. J. Hu, Y. Y. Huang, C. Y. Chen, Y. K. Liu, T. A. Guo, and B. O. Guan, "Highly sensitive detection of dopamine using a graphene functionalized plasmonic fiber-optic sensor with aptamer conformational amplification," Sens. Actuators B **264**, 440–447 (2018).
6. P. Berini, "Long-range surface plasmon polaritons," Adv. Opt. Photon. **1**, 484–588 (2009).
7. J. Homola, "Surface plasmon resonance sensors for detection of chemical and biological species," Chem. Rev. **108**, 462–493 (2008).
8. J. Y. Jing, Q. Wang, W. M. Zhao, and B. T. Wang, "Long-range surface plasmon resonance and its sensing applications: a review," Opt. Laser Eng. **112**, 103–118 (2019).
9. C. T. Yang, L. Wu, P. Bai, and B. Thierry, "Investigation of plasmonic signal enhancement based on long range surface plasmon resonance with gold nanoparticle tags," J. Mater. Chem. C **4**, 9897–9904 (2016).
10. J. Y. Ma, K. Liu, J. F. Jiang, T. H. Xu, S. Wang, P. X. Chang, Z. Zhang, J. H. Zhang, and T. G. Liu, "All optic-fiber coupled plasmon waveguide resonance sensor using ZrS_2 based dielectric layer," Opt. Express **28**, 11280–11289 (2020).
11. A. Shalabney and I. Abdulhalim, "Sensitivity-enhancement methods for surface plasmon sensors," Laser Photon. Rev. **5**, 571–606 (2011).
12. H. T. Zhang, Y. J. Geng, S. P. Xu, W. Q. Xu, Y. Tian, J. Yu, W. Y. Deng, B. Yu, and Y. Liu, "Surface plasmon field-enhanced Raman scattering based on evanescent field excitation of waveguide-coupled surface plasmon resonance configuration," J. Phys. Chem. C **124**, 1640–1645 (2020).
13. J. Y. Jing, Q. Zhu, Z. X. Dai, S. Y. Li, Q. Wang, and W. M. Zhao, "Sensing self-referenced fiber optic long range surface plasmon resonance sensor based on electronic coupling between surface plasmon polaritons," Appl. Opt. **58**, 6329–6334 (2019).
14. Y. Zhao, R. J. Tong, F. Xia, and Y. Peng, "Current status of optical fiber biosensor based on surface plasmon resonance," Biosens. Bioelectron. **142**, 111505 (2019).
15. Y. Liu and W. Peng, "Fiber-optic surface plasmon resonance sensors and biochemical applications: a review," J. Lightwave Technol. **39**, 3781–3791 (2021).
16. C. Caucheteur, T. Guo, and J. Albert, "Review of plasmonic fiber optic biochemical sensors: improving the limit of detection," Anal. Bioanal. Chem. **407**, 3883–3897 (2015).
17. B. D. Gupta and R. Kant, "Recent advances in surface plasmon resonance based fiber optic chemical and biosensors utilizing bulk and nanostructures," Opt. Laser Technol. **101**, 144–161 (2018).
18. Q. L. Duan, Y. N. Liu, S. S. Chang, H. Y. Chen, and J. H. Chen, "Surface plasmonic sensors: sensing mechanism and recent applications," Sensors **21**, 5262 (2021).
19. A. K. Sharma, A. K. Pandey, and B. Kaur, "A review of advancements (2007–2017) in plasmonics-based optical fiber sensors," Opt. Fiber Technol. **43**, 20–34 (2018).
20. M. Chauhan and V. K. Singh, "Review on recent experimental SPR/LSPR based fiber optic analyte sensors," Opt. Fiber Technol. **64**, 102580 (2021).
21. X. D. Wang and O. S. Wolfbeis, "Fiber-optic chemical sensors and biosensors (2015–2019)," Anal. Chem. **92**, 397–430 (2020).
22. M. S. Soares, M. Vidal, N. F. Santos, F. M. Costa, C. Marques, S. O. Pereira, and C. Leitao, "Immunosensing based on optical fiber technology: recent advances," Biosensors **11**, 305 (2021).
23. J. S. Seok and H. Ju, "Plasmonic optical biosensors for detecting C-reactive protein: a review," Micromachines **11**, 895 (2020).
24. M. A. Butt, S. N. Khonina, and N. L. Kazanskiy, "Plasmonics: a necessity in the field of sensing: a review," Fiber Integr. Opt. **40**, 14–47 (2021).
25. S. Lee, H. Song, H. Ahn, S. Kim, J. R. Choi, and K. Kim, "Fiber-optic localized surface plasmon resonance sensors based on nanomaterials," Sensors **21**, 819 (2021).
26. A. Guerreiro, D. F. Santos, and J. M. Baptista, "New trends in the simulation of nanosplasmonic optical D-type fiber sensors," Sensors **19**, 1772 (2019).
27. M. Qi, N. M. Y. Zhang, K. W. Li, S. C. Tjin, and L. Wei, "Hybrid plasmonic fiber-optic sensors," Sensors **20**, 3266 (2020).
28. M. E. Martinez-Hernandez, P. J. Rivero, J. Goicoechea, and F. J. Arregui, "Trends in the implementation of advanced plasmonic materials in optical fiber sensors (2010–2020)," Chemosensors **9**, 64 (2021).
29. B. D. Gupta, A. M. Shrivastav, and S. P. Usha, "Surface plasmon resonance-based fiber optic sensors utilizing molecular imprinting," Sensors **16**, 1381 (2016).
30. T. Yang, X. L. He, X. Zhou, Z. Y. Lei, Y. L. Wang, J. Yang, D. Cai, S. L. Chen, and X. D. Wang, "Surface plasmon cavities on optical fiber end-facets for biomolecule and ultrasound detection," Opt. Laser Technol. **101**, 468–478 (2018).
31. B. Dastmalchi, P. Tassin, T. Koschny, and C. M. Soukoulis, "A new perspective on plasmonics: confinement and propagation length of surface plasmons for different materials and geometries," Adv. Opt. Mater. **4**, 177–184 (2016).
32. S. Shi, L. B. Wang, R. X. Su, B. S. Liu, R. L. Huang, W. Qi, and Z. M. He, "A polydopamine-modified optical fiber SPR biosensor using electroless-plated gold films for immunoassays," Biosens. Bioelectron. **74**, 454–460 (2015).
33. J. Y. Jing, Q. Wang, and B. T. Wang, "Refractive index sensing characteristics of carbon nanotube-deposited photonic crystal fiber SPR sensor," Opt. Fiber Technol. **43**, 137–144 (2018).
34. X. Zhao, X. Zhang, X. S. Zhu, and Y. W. Shi, "Long-range surface plasmon resonance sensor based on the GK570/Ag coated hollow fiber with an asymmetric layer structure," Opt. Express **27**, 9550–9560 (2019).
35. X. Zhang, X. S. Zhu, and Y. W. Shi, "Fiber optic surface plasmon resonance sensor based on a silver-coated large-core suspended-core fiber," Opt. Lett. **44**, 4550–4553 (2019).
36. F. Esposito, L. Sansone, A. Srivastava, F. Baldini, S. Campopiano, F. Chiavaioli, M. Giordano, A. Giannetti, and A. Iadicicco, "Long period grating in double cladding fiber coated with graphene oxide as high-performance optical platform for biosensing," Biosens. Bioelectron. **172**, 112747 (2021).
37. P. Urbancova, M. Goraus, D. Pudis, P. Hlubina, A. Kuzma, D. Jandura, J. Durisova, and P. Micek, "2D polymer/metal structures for surface plasmon resonance," Appl. Surf. Sci. **530**, 147279 (2020).
38. A. Pathak and B. D. Gupta, "Palladium nanoparticles embedded PPy shell coated CNTs towards a high performance hydrazine detection through optical fiber plasmonic sensor," Sens. Actuators B **326**, 128717 (2021).
39. S. T. Wang, N. Liu, Q. Cheng, B. Pang, and J. T. Lv, "Surface plasmon resonance on the antimonene-Fe_2O_3-copper layer for optical attenuated total reflection spectroscopic application," Plasmonics **16**, 559–566 (2020).
40. C. W. Cheng, S. S. Raja, C. W. Chang, X. Q. Zhang, P. Y. Liu, Y. H. Lee, C. K. Shih, and S. Gwo, "Epitaxial aluminum plasmonics covering full visible spectrum," Nanophotonics **10**, 627–637 (2021).
41. M. Kanso, S. Cuenot, and G. Louarn, "Sensitivity of optical fiber sensor based on surface plasmon resonance: modeling and experiments," Plasmonics **3**, 49–57 (2008).
42. P. K. Maharana, R. Jha, and S. Palei, "Sensitivity enhancement by air mediated graphene multilayer based surface plasmon resonance biosensor for near infrared," Sens. Actuators B **190**, 494–501 (2014).

43. F. C. Chien and S. J. Chen, "A sensitivity comparison of optical biosensors based on four different surface plasmon resonance modes," Biosens. Bioelectron. **20**, 633–642 (2004).
44. Y. S. Dwivedi, A. K. Sharma, and B. D. Gupta, "Influence of design parameters on the performance of a surface plasmon sensor based fiber optic sensor," Plasmonics **3**, 79–86 (2008).
45. M. M. Rahman, M. M. Rana, M. S. Rahman, M. S. Anower, M. A. Mollah, and A. K. Paul, "Sensitivity enhancement of SPR biosensors employing heterostructure of $PtSe_2$ and 2D materials," Opt. Mater. **107**, 110123 (2020).
46. H. Agrawal, A. M. Shrivastav, and B. D. Gupta, "Surface plasmon resonance based optical fiber sensor for atrazine detection using molecular imprinting technique," Sens. Actuators B **227**, 204–211 (2016).
47. F. Chiavaioli, C. A. J. Gouveia, P. A. S. Jorge, and F. Baldini, "Towards a uniform metrological assessment of grating-based optical fiber sensors: from refractometers to biosensors," Biosensors **7**, 23 (2017).
48. H. P. Loock and P. D. Wentzell, "Detection limits of chemical sensors: applications and misapplications," Sens. Actuators B **173**, 157–163 (2012).
49. R. Ravikumar, L. H. Chen, P. Jayaraman, C. L. Poh, and C. C. Chan, "Chitosan-nickel film based interferometric optical fiber sensor for label-free detection of histidine tagged proteins," Biosens. Bioelectron. **99**, 578–585 (2018).
50. C. Liu, Q. Cai, B. J. Xu, W. D. Zhu, L. Zhang, J. L. Zhao, and X. F. Chen, "Graphene oxide functionalized long period grating for ultrasensitive label-free immunosensing," Biosens. Bioelectron. **94**, 200–206 (2017).
51. Z. Cheng, Q. Wang, A. S. Zhu, F. M. Qiu, L. Y. Niu, and J. Y. Jing, "Au-nanoshells modified surface field enhanced LRSPR biosensor with low LOD for highly sensitive hIgG sensing," Opt. Laser Technol. **134**, 106656 (2021).
52. Y. Peng, Y. Zhao, X. G. Hu, and Y. Yang, "Optical fiber quantum biosensor based on surface plasmon polaritons for the label-free measurement of protein," Sens. Actuators B **316**, 128097 (2020).
53. J. J. Luo, G. S. Liu, W. J. Zhou, S. Q. Hu, L. Chen, Y. F. Chen, Y. H. Luo, and Z. Chen, "A graphene-PDMS hybrid overcoating enhanced fiber plasmonic temperature sensor with high sensitivity and fast response," J. Mater. Chem. C **8**, 12893–12901 (2020).
54. B. S. Boruah and R. Biswas, "In-situ sensing of hazardous heavy metal ions through an ecofriendly scheme," Opt. Laser Technol. **137**, 106813 (2021).
55. N. Cennamo, G. D'Agostino, M. Pesavento, and L. Zeni, "High selectivity and sensitivity sensor based on MIP and SPR in tapered plastic optical fibers for the detection of L-nicotine," Sens. Actuators B **191**, 529–536 (2014).
56. P. H. Zhang, B. Y. Lu, Y. W. Sun, H. X. Yu, K. X. Xu, and D. C. Li, "Side-polished flexible SPR sensor modified by graphene with *in situ* temperature self-compensation," Biomed. Opt. Express **10**, 215–225 (2019).
57. Q. Wang, H. Song, A. S. Zhu, and F. M. Qiu, "A label-free and anti-interference dual-channel SPR fiber optic sensor with self-compensation for biomarker detection," IEEE Trans. Instrum. Meas. **70**, 7002007 (2021).
58. W. H. Tsai, Y. C. Lin, J. K. Tai, and Y. C. Tsao, "Multi-step structure of side-polished fiber sensor to enhance SPR effect," Opt. Laser Technol. **42**, 453–456 (2010).
59. B. Y. Li, Z. C. Sheng, M. Wu, X. Y. Liu, G. Y. Zhou, J. T. Liu, Z. Y. Hou, and C. M. Xia, "Sensitive real-time monitoring of refractive indices and components using a microstructure optical fiber microfluidic sensor," Opt. Lett. **43**, 5070–5073 (2018).
60. I. Dominguez, I. Del Villar, O. Fuentes, J. M. Corres, and I. R. Matias, "Interdigital concept in photonic sensors based on an array of lossy mode resonances," Sci. Rep. **11**, 13228 (2021).
61. G. L. Xiao, Z. T. Ou, H. Y. Yang, Y. P. Xu, J. Y. Chen, H. O. Li, Q. Li, L. Z. Zeng, Y. R. Den, and J. Q. Li, "An integrated detection based on a multi-parameter plasmonic optical fiber sensor," Sensors **21**, 803 (2021).
62. H. Liu, H. W. Li, Q. Wang, M. Wang, Y. Ding, and C. H. Zhu, "Simultaneous measurement of temperature and magnetic field based on surface plasmon resonance and Sagnac interference in a D-shaped photonic crystal fiber," Opt. Quant. Electron. **50**, 392 (2018).
63. X. C. Yang, Y. Lu, B. L. Liu, and J. Q. Yao, "Simultaneous measurement of refractive index and temperature based on SPR in D-shaped MOF," Appl. Opt. **56**, 4369–4374 (2017).
64. B. Li, F. Zhang, X. Yan, X. N. Zhang, F. Wang, S. G. Li, and T. L. Cheng, "Numerical analysis of dual-parameter optical fiber sensor with large measurement range based on surface plasmon resonance," IEEE Sens. J. **21**, 10719–10725 (2021).
65. T. Ayupova, M. Shaimerdenova, S. Korganbayev, M. Sypabekova, A. Bekmurzayeva, W. Blanc, S. Sales, T. Guo, C. Molardi, and D. Tosi, "Fiber optic refractive index distributed multi-sensors by scattering-level multiplexing with MgO nanoparticle-doped fibers," IEEE Sens. J. **20**, 2504–2510 (2020).
66. M. D. Alonso-Murias, J. S. Velazquez-Gonzalez, and D. Monzon-Hernandez, "SPR fiber tip sensor for the simultaneous measurement of refractive index, temperature, and level of a liquid," J. Lightwave Technol. **37**, 4808–4814 (2019).
67. Q. Wang, J. Y. Jing, X. Z. Wang, L. Y. Niu, and W. M. Zhao, "A D-shaped fiber long-range surface plasmon resonance sensor with high *Q*-factor and temperature self-compensation," IEEE Trans. Instrum. Meas. **69**, 2218–2224 (2020).
68. H. I. Muri, A. Bano, and D. R. Hjelme, "LSPR and interferometric sensor modalities combined using a double-clad optical fiber," Sensors **18**, 187 (2018).
69. T. S. Li, L. Q. Zhu, X. C. Yang, X. P. Lou, and L. D. Yu, "A refractive index sensor based on H-shaped photonic crystal fibers coated with Ag-graphene layers," Sensors **20**, 741 (2020).
70. Z. J. Zhang, Y. Y. Chen, H. J. Liu, H. D. Bae, D. A. Olson, A. K. Gupta, and M. Yu, "On-fiber plasmonic interferometer for multi-parameter sensing," Opt. Express **23**, 10732–10740 (2015).
71. Y. Liu, Q. Xia, A. Zhou, X. B. Wang, and L. B. Yuan, "Multi-parameter sensing based on surface plasma resonance with tungsten disulfide sheets coated," Opt. Express **28**, 6084–6094 (2020).
72. S. J. Weng, L. Pei, C. Liu, J. S. Wang, J. Li, and T. G. Ning, "Double-side polished fiber SPR sensor for simultaneous temperature and refractive index measurement," IEEE Photon. Technol. Lett. **28**, 1916–1919 (2016).
73. Y. Yanase, A. Araki, H. Suzuki, T. Tsutsui, T. Kimura, K. Okamoto, T. Nakatani, T. Hiragun, and M. Hide, "Development of an optical fiber SPR sensor for living cell activation," Biosens. Bioelectron. **25**, 1244–1247 (2010).
74. J. Cao, M. H. Tu, T. Sun, and K. T. V. Grattan, "Wavelength-based localized surface plasmon resonance optical fiber biosensor," Sens. Actuators B **181**, 611–619 (2013).
75. Q. Wang, X. Z. Wang, H. Song, W. M. Zhao, and J. Y. Jing, "A dual channel self-compensation optical fiber biosensor based on coupling of surface plasmon polariton," Opt. Laser Technol. **124**, 106002 (2020).
76. S. Isaacs and I. Abdulhalim, "Long range surface plasmon resonance with ultra-high penetration depth for self-referenced sensing and ultra-low detection limit using diverging beam approach," Appl. Phys. Lett. **106**, 193701 (2015).
77. M. Vala, S. Etheridge, J. A. Roach, and J. Homola, "Long-range surface plasmons for sensitive detection of bacterial analytes," Sens. Actuators B **139**, 59–63 (2009).
78. H. Zhang, Y. F. Chen, X. J. Feng, X. Xiong, S. Q. Hu, Z. P. Jiang, J. L. Dong, W. G. Zhu, W. T. Qiu, H. Y. Guan, H. H. Lu, J. H. Yu, Y. C. Zhong, J. Zhang, M. He, Y. H. Luo, and Z. Chen, "Long-range surface plasmon resonance sensor based on side-polished fiber for biosensing applications," IEEE J. Sel. Top. Quantum Electron. **25**, 7101909 (2019).
79. S. Jain, A. Paliwal, V. Gupta, and M. Tomar, "Refractive index tuning of SiO_2 for long range surface plasmon resonance based biosensor," Biosens. Bioelectron. **168**, 112508 (2020).
80. K. Liu, M. Xue, J. F. Jiang, T. Wang, P. X. Chang, and T. G. Liu, "Theoretical modeling of a coupled plasmon waveguide resonance sensor based on multimode optical fiber," Opt. Commun. **410**, 552–558 (2018).

81. J. Y. Ma, K. Liu, J. F. Jiang, T. H. Xu, S. Wang, P. X. Chang, Z. Zhang, J. H. Zhang, and T. G. Liu, "Theoretical and experimental investigation of an all-fiber waveguide coupled surface plasmon resonance sensor with Au-ZnO-Au sandwich structure," IEEE Access **7**, 169961 (2019).
82. K. Zhang, C. G. Du, and J. C. Gao, "Long-range surface plasmon polariton enhancement in double-electrode structure," Acta Phys. Sinica **66**, 227302 (2017).
83. A. K. Mishra, S. K. Mishra, and R. K. Verma, "Doped single-wall carbon nanotubes in propagating surface plasmon resonance-based fiber optic refractive index sensing," Plasmonics **12**, 1657–1663 (2017).
84. C. Y. Lin and S. J. Chen, "Design of highly sensitive guided-wave surface plasmon resonance biosensor with deep dip using genetic algorithm," Opt. Commun. **445**, 155–160 (2019).
85. V. P. Prakashan, G. George, M. S. Sanu, M. S. Sajna, A. C. Saritha, C. Sudarsanakumar, P. R. Biju, C. Joseph, and N. V. Unnikrishnan, "Investigations on SPR induced Cu@Ag core shell doped SiO_2-TiO_2-ZrO_2 fiber optic sensor for mercury detection," Appl. Surf. Sci. **507**, 144957 (2020).
86. K. X. Dong, Y. P. Ji, J. J. Mi, X. T. Zhao, B. Wu, W. X. Huang, and J. P. Shi, "High sensitivity SPR sensor for liquid phase sample with Ag/PbS/graphene hybrid nanostructure," Opto-Electron. Eng. **44**, 198–201 (2017).
87. X. Y. Xuan, S. P. Xu, Y. Liu, H. B. Li, W. Q. Xu, and J. R. Lombardi, "A long-range surface plasmon resonance/probe/silver nanoparticle (LRSPR-P-NP) nanoantenna configuration for surface-enhanced Raman scattering," J. Phys. Chem. Lett. **3**, 2773–2778 (2012).
88. C. T. Yang, R. Mejard, H. J. Griesser, P. O. Bagnaninchi, and B. Thierry, "Cellular micromotion monitored by long-range surface plasmon resonance with optical fluctuation analysis," Anal. Chem. **87**, 1456–1461 (2015).
89. A. W. Wark, H. J. Lee, and R. M. Corn, "Long-range surface plasmon resonance imaging for bioaffinity sensors," Anal. Chem. **77**, 3904–3907 (2005).
90. Y. Y. Huang, M. F. Ding, T. Guo, D. J. Hu, Y. Y. Cao, L. Jin, and B. O. Guan, "A fiber-optic sensor for neurotransmitters with ultralow concentration: near-infrared plasmonic electromagnetic field enhancement using raspberry-like meso-SiO_2 nanospheres," Nanoscale **9**, 14929–14936 (2017).
91. H. Zhang, Y. Sun, S. Gao, H. Q. Zhang, J. Zhang, Y. Bai, and D. Q. Song, "Studies of gold nanorod-iron oxide nanohybrids for immunoassay based on SPR biosensor," Talanta **125**, 29–35 (2014).
92. S. Shi, L. B. Wang, A. K. Wang, R. L. Huang, L. Ding, R. X. Su, W. Qi, and Z. M. He, "Bioinspired fabrication of optical fiber SPR sensors for immunoassays using polydopamine accelerated electroless plating," J. Mater. Chem. C **4**, 7554–7562 (2016).
93. Q. Wu, Y. Sun, D. Zhang, S. Li, Y. Zhang, P. Y. Ma, Y. Yu, X. H. Wang, and D. Q. Song, "Ultrasensitive magnetic field-assisted surface plasmon resonance immunoassay for human cardiac troponin I," Biosens. Bioelectron. **96**, 288–293 (2017).
94. S. Li, Q. Wu, P. Y. Ma, Y. Zhang, D. Q. Song, X. H. Wang, and Y. Sun, "A sensitive SPR biosensor based on hollow gold nanospheres and improved sandwich assay with PDA-Ag@Fe_3O_4/rGO," Talanta **180**, 156–161 (2018).
95. C. Fenzl, T. Hirsch, and A. J. Baeumner, "Liposomes with high refractive index encapsulants as tunable signal amplification tools in surface plasmon resonance spectroscopy," Anal. Chem. **87**, 11157–11163 (2015).
96. H. Komatsu, M. Miyachi, E. Fujii, D. Citterio, K. Yamada, Y. Sato, K. Kurihara, H. Kawaguchi, and K. Suzuki, "SPR sensor signal amplification based on dye-doped polymer particles," Sci. Technol. Adv. Mater. **7**, 150–155 (2006).
97. X. H. Zhu, Y. Y. Zhang, M. L. Liu, and Y. Liu, "2D titanium carbide MXenes as emerging optical biosensing platforms," Biosens. Bioelectron. **171**, 112730 (2021).
98. L. Y. Niu, Q. Wang, J. Y. Jing, and W. M. Zhao, "Sensitivity enhanced D-type large-core fiber SPR sensor based on Gold nanoparticle/Au film co-modification," Opt. Commun. **450**, 287–295 (2019).
99. H. Z. Yuan, W. Ji, S. W. Chu, S. Y. Qian, F. Wang, J. F. Masson, X. Y. Han, and W. Peng, "Fiber-optic surface plasmon resonance glucose sensor enhanced with phenylboronic acid modified Au nanoparticles," Biosens. Bioelectron. **117**, 637–643 (2018).
100. K. Liu, J. H. Zhang, J. F. Jiang, T. H. Xu, S. Wang, P. X. Chang, Z. Zhang, J. Y. Ma, and T. G. Liu, "Multi-layer optical fiber surface plasmon resonance biosensor based on a sandwich structure of polydopamine-$MoSe_2$@Au nanoparticles-polydopamine," Biomed. Opt. Express **11**, 6840–6851 (2020).
101. A. M. Shrivastav, S. P. Usha, and B. D. Gupta, "Highly sensitive and selective erythromycin nanosensor employing fiber optic SPR/ERY imprinted nanostructure: application in milk and honey," Biosens. Bioelectron. **90**, 516–524 (2017).
102. H. Song, H. X. Zhang, Z. Sun, Z. Y. Ren, X. Y. Yang, and Q. Wang, "Triangular silver nanoparticle U-bent fiber sensor based on localized surface plasmon resonance," AIP Adv. **9**, 085307 (2019).
103. M. Sun, Y. X. Wang, Z. N. Chen, Y. D. Gong, J. L. Lim, and X. M. Qing, "Nanostars on a fiber facet with near field enhancement for surface-enhanced Raman scattering detection," Appl. Phys. A **115**, 87–91 (2014).
104. F. Xia, H. Song, Y. Zhao, W. M. Zhao, Q. Wang, X. Z. Wang, B. T. Wang, and Z. X. Dai, "Ultra-high sensitivity SPR fiber sensor based on multilayer nanoparticle and Au film coupling enhancement," Measurement **164**, 108083 (2020).
105. D. J. Feng, G. X. Liu, Q. Li, J. Cui, J. Zheng, and Z. C. Ye, "Design of infrared SPR sensor based on bimetallic nanowire gratings on plastic optical fiber surface," IEEE Sens. J. **15**, 255–259 (2015).
106. R. Kant, R. Tabassum, and B. D. Gupta, "Xanthine oxidase functionalized Ta_2O_5 nanostructures as a novel scaffold for highly sensitive SPR based fiber optic xanthine sensor," Biosens. Bioelectron. **99**, 637–645 (2018).
107. S. Parveen, A. Pathak, and B. D. Gupta, "Fiber optic SPR nanosensor based on synergistic effects of CNT/Cu-nanoparticles composite for ultratrace sensing of nitrate," Sens. Actuators B **246**, 910–919 (2017).
108. X. Jiang and Q. Wang, "Refractive index sensitivity enhancement of optical fiber SPR sensor utilizing layer of MWCNT/PtNPs composite," Opt. Fiber Technol. **51**, 118–124 (2019).
109. A. V. Kabashin, P. Evans, S. Pastkovsky, W. Hendren, G. A. Wurtz, R. Atkinson, R. Pollard, V. A. Podolskiy, and A. V. Zayats, "Plasmonic nanorod metamaterials for biosensing," Nat. Mater. **8**, 867–871 (2009).
110. Y. N. Zhang, B. R. Tao, Q. L. Wu, and B. Han, "Reflective SPR sensor for simultaneous measurement of nitrate concentration and temperature," IEEE Trans. Instrum. Meas. **68**, 4566–4573 (2019).
111. A. Pathak, S. Parveen, and B. D. Gupta, "Fibre optic SPR sensor using functionalized CNTs for the detection of SMX: comparison with enzymatic approach," Plasmonics **13**, 189–202 (2018).
112. A. Pathak and B. D. Gupta, "Ultra-selective fiber optic SPR platform for the sensing of dopamine in synthetic cerebrospinal fluid incorporating permselective nafion membrane and surface imprinted MWCNTs-PPy matrix," Biosens. Bioelectron. **133**, 205–214 (2019).
113. S. K. Mishra, S. N. Tripathi, V. Choudhary, and B. D. Gupta, "Surface plasmon resonance-based fiber optic methane gas sensor utilizing graphene-carbon nanotubes-poly(methyl methacrylate) hybrid nanocomposite," Plasmonics **10**, 1147–1157 (2015).
114. R. Tabassum and B. D. Gupta, "Simultaneous tuning of electric field intensity and structural properties of ZnO: graphene nanostructures for FOSPR based nicotine sensor," Biosens. Bioelectron. **91**, 762–769 (2017).
115. B. T. Wang, Y. X. Niu, S. W. Zheng, Y. H. Yin, and M. Ding, "An optical fiber immunosensor with a low detection limit based on plasmon coupling enhancement," J. Lightwave Technol. **38**, 3781–3788 (2020).
116. W. Yang, J. Yu, X. T. Xi, Y. Sun, Y. M. Shen, W. W. Yue, C. Zhang, and S. Z. Jiang, "Preparation of graphene/ITO nanorod metamaterial/U-bent-annealing fiber sensor and DNA biomolecule detection," Nanomaterials **9**, 1154 (2019).
117. A. K. Pathak and V. K. Singh, "SPR based optical fiber refractive index sensor using silver nanowire assisted CSMFC," IEEE Photon. Technol. Lett. **32**, 465–468 (2020).

118. Y. Guo, J. S. Li, S. G. Li, Y. D. Liu, S. H. Zhang, J. Wang, S. Wang, W. X. Zhang, T. L. Cheng, and R. Hao, "Dual-polarized optical sensing of microstructure fiber with pentagonal-lattice based on surface plasmon resonance in the near-IR spectrum," Optik **202**, 163671 (2020).
119. Q. Wu, N. B. Li, Y. Wang, Y. C. Xu, J. D. Wu, G. R. Jia, F. J. Ji, X. D. Fang, F. F. Chen, and X. Q. Cui, "Ultrasensitive and selective determination of carcinoembryonic antigen using multifunctional ultrathin amino-functionalized Ti_3C_2-MXene nanosheets," Anal. Chem. **92**, 3354–3360 (2020).
120. L. X. Kang, C. M. Das, D. Liu, M. W. Chen, P. Coquet, G. Hong, and K. T. Yong, "A comparative performance evaluation of 2D nanomaterials for applications in plasmonic biosensing," Phys. Status Solidi A **217**, 2000255 (2020).
121. N. Li, J. J. Guo, Y. W. Ding, Y. Q. Hu, C. H. Zhao, and C. J. Zhao, "Direct regulation of double cation defects at the A1A2 site for a high-performance oxygen evolution reaction perovskite catalyst," ACS Appl. Mater. Interfaces **13**, 332–340 (2021).
122. D. T. Nurrohman, Y. H. Wang, and N. F. Chiu, "Exploring graphene and MoS_2 chips based surface plasmon resonance biosensors for diagnostic applications," Front. Chem. **8**, 728 (2020).
123. R. Kumar, S. Pal, A. Verma, Y. K. Prajapati, and J. P. Saini, "Effect of silicon on sensitivity of SPR biosensor using hybrid nanostructure of black phosphorus and MXene," Superlattices Microstruct. **145**, 106591 (2020).
124. Y. F. Yuan, X. T. Yu, Q. L. Ouyang, Y. H. Shao, J. Song, J. L. Qu, and K. T. Yong, "Highly anisotropic black phosphorous-graphene hybrid architecture for ultrassensitive plasmonic biosensing: theoretical insight," 2D Mater. **5**, 025015 (2018).
125. H. Song, Q. Wang, and W. M. Zhao, "A novel SPR sensor sensitivity-enhancing method for immunoassay by inserting MoS_2 nanosheets between metal film and fiber," Opt. Laser Eng. **132**, 106135 (2020).
126. S. Pal, A. Verma, Y. K. Prajapati, and J. P. Saini, "Sensitive detection using heterostructure of black phosphorus, transition metal di-chalcogenides and MXene in SPR sensor," Appl. Phys. A **126**, 809 (2020).
127. M. S. Rahman, M. S. Anower, and L. F. Abdulrazak, "Utilization of a phosphorene-graphene/TMDC heterostructure in a surface plasmon resonance-based fiber optic biosensor," Photon. Nanostr. Fundam. Appl. **35**, 100711 (2019).
128. Y. Z. Chen, Y. Q. Ge, W. C. Huang, Z. J. Li, L. M. Wu, H. Zhang, and X. J. Li, "Refractive index sensors based on $Ti_3C_2T_x$ MXene fibers," ACS Appl. Nano Mater. **3**, 303–311 (2020).
129. Z. C. Xia, F. H. Chu, Z. L. Bian, Z. Zhang, J. L. Li, and Z. Guo, "Study of surface plasmon resonance sensor based on polymer-tipped optical fiber with barium titanate layer," J. Lightwave Technol. **38**, 912–918 (2020).
130. Y. Vasimalla, H. S. Pradhan, and R. J. Pandya, "SPR performance enhancement for DNA hybridization employing black phosphorus, silver, and silicon," Appl. Opt. **59**, 7299–7307 (2020).
131. Q. Wu, N. B. Li, Y. Wang, Y. Liu, Y. C. Xu, S. T. Wei, J. D. Wu, G. R. Jia, X. D. Fang, F. F. Chen, and X. Q. Cui, "A 2D transition metal carbide MXene-based SPR biosensor for ultrasensitive carcinoembryonic antigen detection," Biosens. Bioelectron. **144**, 111697 (2019).
132. N. Mudgal, P. Yupapin, J. Ali, and G. Singh, "$BaTiO_3$-graphene-affinity layer-based surface plasmon resonance (SPR) biosensor for pseudomonas bacterial detection," Plasmonics **15**, 1221–1229 (2020).
133. A. Srivastava, R. Das, and Y. K. Prajapati, "Effect of perovskite material on performance of surface plasmon resonance biosensor," IET Optoelectron. **14**, 256–265 (2020).
134. M. Alagdar, B. Yousif, N. F. Areed, and M. Elzalabani, "Highly sensitive fiber optic surface plasmon resonance sensor employing 2D nanomaterials," Appl. Phys. A **126**, 522 (2020).
135. Vikas, M. K. Yadav, P. Kumar, and R. K. Verma, "Detection of adulteration in pure honey utilizing Ag-graphene oxide coated fiber optic SPR probes," Food Chem. **332**, 127346 (2020).
136. Q. Wang, X. Jiang, L. Y. Niu, and X. C. Fan, "Enhanced sensitivity of bimetallic optical fiber SPR sensor based on MoS_2 nanosheets," Opt. Laser Eng. **128**, 105997 (2020).
137. S. Kaushik, U. K. Tiwari, A. Deep, and R. K. Sinha, "Two-dimensional transition metal dichalcogenides assisted biofunctionalized optical fiber SPR biosensor for efficient and rapid detection of bovine serum albumin," Sci. Rep. **9**, 6987 (2019).
138. K. Liu, J. H. Zhang, J. F. Jiang, T. H. Xu, S. Wang, P. X. Chang, Z. Zhang, J. Y. Ma, and T. G. Liu, "$MoSe_2$-Au Based sensitivity enhanced optical fiber surface plasmon resonance biosensor for detection of goat-anti-rabbit IgG," IEEE Access **8**, 660–668 (2020).
139. A. K. Mishra, S. K. Mishra, and R. K. Verma, "Graphene and beyond graphene MoS_2: a new window in surface-plasmon-resonance-based fiber optic sensing," J. Phys. Chem. C **120**, 2893–2900 (2016).
140. A. K. Sharma, A. K. Pandey, and B. Kaur, "Simulation study on comprehensive sensing enhancement of BlueP/MoS_2-and BlueP/WS2-based fluoride fiber surface plasmon resonance sensors: analysis founded on damping, field, and optical power," Appl. Opt. **58**, 4518–4525 (2019).
141. M. S. Rahman, M. S. Anower, and L. F. Abdulrazak, "Modeling of a fiber optic SPR biosensor employing tin selenide (SnSe) allotropes," Results Phys. **15**, 102623 (2019).
142. S. Sharma and B. D. Gupta, "Surface plasmon resonance based highly selective fiber optic dopamine sensor fabricated using molecular imprinted GNP/SnO_2 nanocomposite," J. Lightwave Technol. **36**, 5956–5962 (2018).
143. R. Kant and B. D. Gupta, "Fiber-optic SPR based acetylcholine biosensor using enzyme functionalized Ta_2O_5 nanoflakes for Alzheimer's disease diagnosis," J. Lightwave Technol. **36**, 4018–4024 (2018).
144. Vikas and R. K. Verma, "On the application of few layer Ti_3C_2 MXene on fiber optic SPR sensor for performance enhancement," Eur. Phys. J. D **75**, 5 (2021).
145. Q. Wang, L. Y. Niu, J. Y. Jing, and W. M. Zhao, "Barium titanate film based fiber optic surface plasmon sensor with high sensitivity," Opt. Laser Technol. **124**, 105899 (2020).
146. S. H. Sun, C. B. Murray, D. Weller, L. Folks, and A. Moser, "Monodisperse FePt nanoparticles and ferromagnetic FePt nanocrystal superlattices," Science **287**, 1989–1992 (2000).
147. N. A. Sakthivel and A. Dass, "Aromatic thiolate-protected series of gold nanomolecules and a contrary structural trend in size evolution," Acc. Chem. Res. **51**, 1774–1783 (2018).
148. H. Wu, F. Bai, Z. C. Sun, R. E. Haddad, D. M. Boye, Z. W. Wang, J. Y. Huang, and H. Y. Fan, "Nanostructured gold architectures formed through high pressure-driven sintering of spherical nanoparticle arrays," J. Am. Chem. Soc. **132**, 12826–12828 (2010).
149. J. J. Cheng, G. Le Saux, J. Gao, T. Buffeteau, Y. Battie, P. Barois, V. Ponsinet, M. H. Delville, O. Ersen, E. Pouget, and R. Oda, "GoldHelix: gold nanoparticles forming 3D helical superstructures with controlled morphology and strong chiroptical property," ACS Nano **11**, 3806–3818 (2017).
150. C. Li, Z. Li, S. L. Li, Y. N. Zhang, B. P. Sun, Y. H. Yu, H. Y. Ren, S. Z. Jiang, and W. W. Yue, "LSPR optical fiber biosensor based on a 3D composite structure of gold nanoparticles and multilayer graphene films," Opt. Express **28**, 6071–6083 (2020).
151. D. Daems, W. Pfeifer, I. Rutten, B. Sacca, D. Spasic, and J. Lammertyn, "Three-dimensional DNA origami as programmable anchoring points for bioreceptors in fiber optic surface plasmon resonance biosensing," ACS Appl. Mater. Interfaces **10**, 23539–23547 (2018).
152. Y. Zhao, M. Lei, S. X. Liu, and Q. Zhao, "Smart hydrogel-based optical fiber SPR sensor for pH measurements," Sens. Actuators B **261**, 226–232 (2018).
153. L. X. Kong, Y. X. Zhang, W. G. Zhang, Y. S. Zhang, T. Y. Yan, P. C. Geng, and B. Wang, "Lab-on-tip: protruding-shaped all-fiber plasmonic microtip probe toward *in-situ* chem-bio detection," Sens. Actuators B **301**, 127128 (2019).
154. S. J. Guo and S. J. Dong, "Metal nanomaterial-based self-assembly: development, electrochemical sensing and SERS applications," J. Mater. Chem. **21**, 16704–16716 (2011).
155. P. Colson, C. Henrist, and R. Cloots, "Nanosphere lithography: a powerful method for the controlled manufacturing of nanomaterials," J. Nanomater. **2013**, 948510 (2013).

156. Y. Wang, Z. J. Cui, X. J. Zhang, X. Zhang, Y. Q. Zhu, S. G. Chen, and H. Hu, "Excitation of surface plasmon resonance on multiwalled carbon nanotube metasurfaces for pesticide sensors," ACS Appl. Mater. Interfaces **12**, 52082–52088 (2020).
157. Q. Wang and L. Wang, "Lab-on-fiber: plasmonic nano-arrays for sensing," Nanoscale **12**, 7485–7499 (2020).
158. V. G. Kravets, A. V. Kabashin, W. L. Barnes, and A. N. Grigorenko, "Plasmonic surface lattice resonances: a review of properties and applications," Chem. Rev. **118**, 5912–5951 (2018).
159. X. L. He, H. Yi, J. Long, X. Zhou, J. Yang, and T. Yang, "Plasmonic crystal cavity on single-mode optical fiber end facet for label-free biosensing," Appl. Phys. Lett. **108**, 231105 (2016).
160. I. Antohe, D. Spasic, F. Delport, J. Q. Li, and J. Lammertyn, "Nanoscale patterning of gold-coated optical fibers for improved plasmonic sensing," Nanotechnology **28**, 215301 (2017).
161. N. Wang, M. Zeisberger, U. Hubner, and M. A. Schmidt, "Nanotrimer enhanced optical fiber tips implemented by electron beam lithography," Opt. Mater. Express **8**, 2246–2255 (2018).
162. C. Ciraci, R. T. Hill, J. J. Mock, Y. Urzhumov, A. I. Fernandez-Dominguez, S. A. Maier, J. B. Pendry, A. Chilkoti, and D. R. Smith, "Probing the ultimate limits of plasmonic enhancement," Science **337**, 1072–1074 (2012).
163. W. Q. Zhu, R. Esteban, A. G. Borisov, J. J. Baumberg, P. Nordlander, H. J. Lezec, J. Aizpurua, and K. B. Crozier, "Quantum mechanical effects in plasmonic structures with subnanometre gaps," Nat. Commun. **7**, 11495 (2016).
164. J. J. Baumberg, J. Aizpurua, M. H. Mikkelsen, and D. R. Smith, "Extreme nanophotonics from ultrathin metallic gaps," Nat. Mater. **18**, 668–678 (2019).
165. C. Lee, B. Lawrie, R. Pooser, K. G. Lee, C. Rockstuhl, and M. Tame, "Quantum plasmonic sensors," Chem. Rev. **121**, 4743–4804 (2021).
166. S. Kim, N. Yu, X. Z. Ma, Y. Z. Zhu, Q. S. Liu, M. Liu, and R. X. Yan, "High external-efficiency nanofocusing for lens-free near-field optical nanoscopy," Nat. Photonics **13**, 636–643 (2019).
167. M. Danckwerts and L. Novotny, "Optical frequency mixing at coupled gold nanoparticles," Phys. Rev. Lett. **98**, 026104 (2007).
168. P. Anger, P. Bharadwaj, and L. Novotny, "Enhancement and quenching of single-molecule fluorescence," Phys. Rev. Lett. **96**, 113002 (2006).
169. X. L. He, L. Yang, and T. Yang, "Optical nanofocusing by tapering coupled photonic-plasmonic waveguides," Opt. Express **19**, 12865–12872 (2011).
170. C. M. Miyazaki, D. J. Kinahan, R. Mishra, F. Mangwanya, N. Kilcawley, M. Ferreira, and J. Ducree, "Label-free, spatially multiplexed SPR detection of immunoassays on a highly integrated centrifugal lab-on-a-disc platform," Biosens. Bioelectron. **119**, 86–93 (2018).
171. M. Q. Zou, C. R. Liao, S. Liu, C. Xiong, C. Zhao, J. L. Zhao, Z. S. Gan, Y. P. Chen, K. M. Yang, D. Liu, Y. Wang, and Y. P. Wang, "Fiber-tip polymer clamped-beam probe for high-sensitivity nanoforce measurements," Light Sci. Appl. **10**, 171 (2021).
172. T. Q. Zhang, M. D. Wang, Y. Xue, J. L. Xu, Z. D. Xie, and S. N. Zhu, "Liquid metal as a broadband saturable absorber for passively Q-switched lasers," Chin. Opt. Lett. **18**, 111801 (2020).
173. R. T. Liu, X. Y. Ye, and T. H. Cui, "Recent progress of biomarker detection sensors," Research **2020**, 7949037 (2020).
174. P. X. Chang, K. Liu, J. F. Jiang, T. H. Xu, Z. Zhang, J. Y. Ma, Y. H. Zhao, J. H. Zhang, X. B. Li, and T. G. Liu, "The temperature responsive mechanism of fiber surface plasmon resonance sensor," Sens. Actuators A Phys. **309**, 112022 (2020).
175. L. M. Wu, Z. T. Ling, L. Y. Jiang, J. Guo, X. Y. Dai, Y. J. Xiang, and D. Y. Fan, "Long-range surface plasmon with graphene for enhancing the sensitivity and detection accuracy of biosensor," IEEE Photon. J. **8**, 4801409 (2016).